

## One-, two-, and three-particle distributions in $pp$ collisions at 205 GeV/c

T. Kafka, R. Engelmann, R. Godbole, J. Hanlon, M. Pratap,\* and H. Wahl†  
*State University of New York, Stony Brook, New York 11794*‡

R. Singer, Y. Cho, T. Fields, and L. G. Hyman  
*Argonne National Laboratory, Argonne, Illinois 60439*§

L. Voyvodic, R. Walker, and J. Whitmore\*  
*Fermi National Accelerator Laboratory, Batavia, Illinois 60510*§  
 (Received 2 December 1976)

Results of a Fermilab experiment using the 30-in. hydrogen bubble chamber are reported, with the main emphasis on pion production in the central region. Single-particle inclusive and semi-inclusive distributions in rapidity, Feynman  $x$ , and  $p_T^2$  for both  $\pi^-$  and  $\pi^+$  are presented and compared with results of other experiments. Two-particle distributions are investigated using the correlation-function formalism. The relation between inclusive and semi-inclusive correlation functions is discussed. The semi-inclusive correlation functions in rapidity are found to have short-range character compatible with the ideas of independent-cluster-emission models. Evidence for effects due to Bose-Einstein statistics of like particles is found by comparing the joint correlation function in rapidity and azimuthal angle, as well as the charged multiplicity associated with transverse momentum in the like- and unlike-charge combinations. Data on the average associated transverse momentum are also presented. The inclusive and semi-inclusive three-particle distributions are presented for all charge combinations. The inclusive three-particle correlations are found to be small for events with more than four particles in the final state. Two independent ways were found in which three-particle densities can be expressed in terms of one- and two-particle densities.

### I. INTRODUCTION

Production of multiparticle final states in high-energy hadron collisions has been studied for some time, with the early data coming from cosmic-ray experiments. In the recent past, the CERN Intersecting Storage Rings (ISR) and the Fermi National Accelerator Laboratory (Fermilab) have provided opportunities to obtain more quantitative data on hadron interactions in an energy region where the average number of particles produced in an inelastic collision is ten or larger.

Because of the complexity of investigating a reaction with a final state of  $N$  particles with its  $(3N-4)$  independent kinematic variables, a theoretical, or at least phenomenological, framework is desirable to indicate which combinations of experimental observables are of most direct physical interest. We refer to appropriate review papers<sup>1</sup> for a summary of current models of multiparticle production. Many of these models can be usefully tested using inclusive distributions, in which only a few particles are considered at a time.

The data presented in this report were obtained by analyzing a sample of 5000 inelastic 205-GeV/c proton-proton interactions observed in the 30-in. hydrogen bubble chamber at Fermilab. Results from this exposure concerning many aspects of the data have been published previously: charged multiplicity distribution,<sup>2,3</sup> elastic scattering,<sup>4</sup> inclusive distributions of the identified slow protons and

the diffractive events,<sup>5-9</sup> the  $pp\pi^+\pi^-$  final state,<sup>10,11</sup> production of neutral secondary particles,<sup>12-14</sup> inclusive  $\pi^-$  distributions,<sup>15-17</sup> various correlations,<sup>18-22</sup> charge-transfer and hemisphere multiplicities,<sup>23</sup> rapidity-gap distributions,<sup>24</sup> and resonance production [ $\Delta^{++}$  (Ref. 25),  $\rho^0$  (Ref. 26)]. In the present paper we restrict our attention to those features of the data for which measurement of all charged particles in each event is necessary. We present the following results:

(i) single-particle inclusive distributions, from the reaction

$$p + p \rightarrow \pi^\alpha + \text{anything},$$

in Sec. III,

(ii) two-particle inclusive distributions, from the reaction

$$p + p \rightarrow \pi^\alpha + \pi^\beta + \text{anything},$$

in Sec. IV, and

(iii) three-particle inclusive distributions, from the reaction

$$p + p \rightarrow \pi^\alpha + \pi^\beta + \pi^\gamma + \text{anything}$$

in Sec. V.

Here  $\alpha$ ,  $\beta$ , and  $\gamma$  denote the charge of the particle included in the distribution:  $\alpha = +$  ( $-$ ), if only positive (negative) particles are included, and  $\alpha = c$  (for "charged") if both positive and negative particles are included. Inclusive distributions for events with a fixed multiplicity of charged secondaries ("semi-inclusive distributions") are also

presented.

The bubble-chamber technique is well suited for inclusive studies, since its  $4\pi$  solid-angle acceptance and its small biases for events with many outgoing particles are difficult to achieve with other kinds of experimental arrangements. Another advantage over many counter experiments is the fact that the sensitive volume of the bubble chamber is placed in a magnetic field which serves the dual purpose of momentum measurement and determination of the sign of electric charge of all observed particles.

## II. DATA ACQUISITION

### A. Film exposure

The 30-in. bubble chamber filled with liquid hydrogen was exposed to a beam of 205-GeV/ $c$  protons at the Fermi National Accelerator Laboratory. This was the first experiment for both the bubble chamber and the external proton beam at the Fermilab. The run was made in two parts. In the first part, an extracted 205-GeV/ $c$  proton beam was strongly attenuated in intensity by a series of defocusing quadrupoles, and then, after a total transport length of about 1 km, traversed the bubble chamber directly. For the second part, a 300-GeV/ $c$  proton beam struck an external target from which a secondary beam (production angle  $\approx 2$  mrad) was transported to the bubble chamber. Contamination of the beam by either pions or leptons was very small under both experimental arrangements, and is neglected in our analysis.

32 000 (35 000) pictures were taken during the first (second) part of the exposure with an average of 3.5 (5.5) beam tracks per picture. (Only 15 000 pictures from the first part of the exposure were usable for physics analysis.) The magnetic field in the bubble chamber was 27 kG (30 kG). During both parts of the experiment, four views of the bubble chamber were photographed on a single strip of 70-mm film.

### B. Scanning

The film was scanned twice using projectors with images about the actual size of the illuminated volume of the bubble chamber. An additional high-magnification scan (images six times larger) was performed by physicists to resolve events with overlapping tracks, events with secondary interactions or decays of neutral secondary particles close to the primary vertex, etc.

The bubble-chamber volume in which events were accepted ("fiducial volume") was limited to a region of length 40 cm along the beam direction, located in the upstream part of the chamber. The scanning efficiency for events with four or more charged

prongs was  $(98.7 \pm 1.0)\%$ .<sup>3</sup> For the two-prong events, the scanning efficiency was  $(98 \pm 2)\%$ ,<sup>4</sup> excluding events with a short (less than 2-mm) re-coil-proton track.

### C. Track measurement and reconstruction

The low- and the high-multiplicity events were treated in different ways. All two- and four-prong events were measured with the ANL semiautomatic measuring system POLLY III.<sup>27</sup> Events which failed this first measurement were then remeasured manually using the high-magnification projection. All tracks were reconstructed in space using the standard three-view geometry program TVGP.<sup>28</sup> All two-prong events were then processed by the kinematic-fitting program SQUAW<sup>29</sup> in order to separate elastic from inelastic events.<sup>4</sup> This separation cannot be done exactly because of the poor momentum resolution of the fast forward-going particle. However, the loss of inelastic two-prong events and the contamination of the inelastic sample by elastic events have a negligible effect on the results presented here, since two-prong events contribute only 2.5% of the tracks to the inclusive sample.

For a successful reconstruction in space, each track must be identified in at least two views. The usual procedure at lower energies is to measure tracks in each view independently and then match the views with the help of an appropriate track-matching algorithm. However, this procedure is unfeasible in our experiment, because most events are characterized by fast secondary particles confined to a cone with a very narrow opening angle. The images of the fast tracks are close to each other, often one overlapping each other, and automatic computer matching was found to be unsuccessful. A method of matching tracks in different views by eye was therefore developed.<sup>30</sup> In this procedure, the high-magnification projection was used. In the first view, the scanner located a suitable region where the tracks were separated from one another. In this region, each bubble of all tracks was traced on a sheet of paper, and each track was labeled by a number. In the second view, the tracks were recognized by their bubble pattern, the event was sketched again, and the tracks were marked with numbers corresponding to those in the first view. When measuring, the operator processed the tracks in the sequence given by the labels in the sketch for the appropriate view.

In order to check the computer matching used for the two- and four-prong events, 250 four-prong events were measured using the bubble-pattern matching method (two-view reconstruction) and

compared with the same events processed using the computer matching (three-view reconstruction). Results of both measurement methods were consistent with one another.

The fiducial volume for the measurement of six-, eight-, and ten-prong events was the same as the fiducial volume for scanning. For higher multiplicities the fiducial volume was shortened to about 34 cm to allow for separation of tracks in the forward cone.

The events with six or more prongs were measured using image-plane digitizers (IPD's, average setting error of 14  $\mu\text{m}$  on the film) and film-plane digitizers (FPD's, average setting error of 8  $\mu\text{m}$ ). The tracks were then reconstructed using the standard reconstruction program TVGP. In a given event, only those tracks that failed reconstruction were remeasured. These were tracks which had a root-mean-square deviation of the measured points from the best fit of the particle's trajectory on film larger than 25  $\mu\text{m}$  (35  $\mu\text{m}$ ) when measured on an FPD (IPD), or larger than 20  $\mu\text{m}$  when measured at large magnification. About two-thirds of the total number of scanned events were accepted for measurement. The remaining events were rejected for such reasons as missing views, events out of the fiducial volume, overlapping tracks, secondary interactions too close to the primary vertex, etc. Up to four measurement passes were performed when necessary, with about 99% of the tracks (about 95% of the events) finally passing the reconstruction criterion.

Table I lists the number of events of each multiplicity included in the following analysis. Each multiplicity was assigned a weight to obtain the correct multiplicity distribution with six-prong

events being given a weight of one. The weights are listed in Table I along with the correct multiplicity distribution from Ref. 3.

The nominal value of  $p_{\text{beam}} = (205.0 \pm 1.0) \text{ GeV}/c$  was used for the beam momentum. The average azimuthal and dip angles,  $\phi_{\text{beam}} = 179.853^\circ \pm 0.035^\circ$  and  $\lambda_{\text{beam}} = -0.288^\circ \pm 0.003^\circ$ , determined by measuring a sample of throughgoing beam tracks, were assigned to the beam track in each event.

The average relative error in the magnitude of the laboratory momentum,  $p$ , is shown in Fig. 1 as a function of  $p$  for those tracks for which the momentum magnitude was used in the data analysis. (Tracks with  $\Delta p/p > 0.75$  are not included, so that the curve in Fig. 1 underestimates the overall momentum error for  $p > 40 \text{ GeV}/c$ .)

To determine the accuracy with which certain kinematic variables were measured, repeated measurements were performed on a random sample of tracks. In addition, errors of these variables were determined using the errors in momentum magnitude and in the azimuthal and dip angles calculated by the reconstruction program TVGP. The variables in question are defined as follows:

(i) Rapidity:

$$y \equiv \frac{1}{2} \ln \frac{E + p_l}{E - p_l},$$

where  $E$  and  $p_l$  are the particle's energy and longitudinal momentum in the desired coordinate system. To compare our data with results of other experiments we also use the pseudorapidity,  $\eta \equiv -\frac{1}{2} \ln(\tan \frac{1}{2} \theta)$ , where  $\theta$  is the particle's production angle. For zero-mass particles,  $\eta = y$ .

(ii) The Feynman scaling variable,  $x$ :

TABLE I. Number of events in the data sample for each multiplicity.

Multiplicity	Number of events scanned (from Ref. 3)	Number of events measured and used in the analysis $N_n$	Weight $w_n$
2	598	586	0.81
(inelastic)			
4	1396	1134	0.84
6	1629	1085	1.00
8	1354	871	1.02
10	1077	578	1.23
12	763	344	1.43
14	373	161	1.54
16	200	66	2.04
18	79	32	1.67
20	28	8	1.80
22	12	3	2.89
Total	7514	$\sum_n N_n = 5036$	$\sum_n N_n w_n = 5282.5$

$$x \equiv \frac{2p_{1c.m.}}{\sqrt{s}}$$

Here  $p_{1c.m.}$  is the particle's longitudinal momentum in the center-of-mass system (c.m.s.) and  $\sqrt{s}$  is the total center-of-mass (c.m.) energy of the colliding particles. For 205-GeV/c proton-proton collisions,  $\sqrt{s} = 19.7$  GeV.

(iii) The angle between transverse momentum vectors ( $\vec{p}_T$ ) of the two particles:

$$\phi \equiv \cos^{-1} \frac{\vec{p}_{T1} \cdot \vec{p}_{T2}}{|\vec{p}_{T1}| |\vec{p}_{T2}|}$$

Table II gives typical errors in the rapidity, the magnitude of the transverse momentum, and the  $x$  variable. The relative errors in the angle  $\phi$  are  $\Delta\phi/\phi \approx 20\%$  for small values of  $\phi$ ,  $\approx 5\%$  for  $\phi$  around  $90^\circ$ , and  $\geq 20\%$  for  $\phi$  close to  $180^\circ$ .

#### D. Mass and charge assignment

The calculation of the energy of a particle, and as a consequence its rapidity and  $x$  values, requires mass identification. However, the capability of a bubble chamber as an instrument for determination of a particle's mass is confined to a limited region of phase space. In the remaining part of phase space one has to make a judicious choice. It is known from other experiments<sup>31</sup> that over 80% of the secondary particles in high-energy hadron collisions are pions, and therefore it is customary to assign a particle the pion mass when its identity is unknown.

The following mass assignments were made in this experiment. All negative particles were assumed to be  $\pi^-$ . Positive particles with momenta less than 1.4 GeV/c were identified by their ionization as either protons or  $\pi^+$ . Positive particles with momenta between 1.4 and 120 GeV/c were assigned the pion mass. (We estimate that in this region  $\approx 14\%$  of the positive particles are protons.) All positive particles with  $p_{lab} > 120$  GeV/c ( $x > 0.6$ ) were assigned the proton mass for the following reason. From our ionization results we find that the fraction of positive pions with  $x < -0.6$  (Ref. 32) is 1.3%. The symmetry of the  $pp$  system ensures

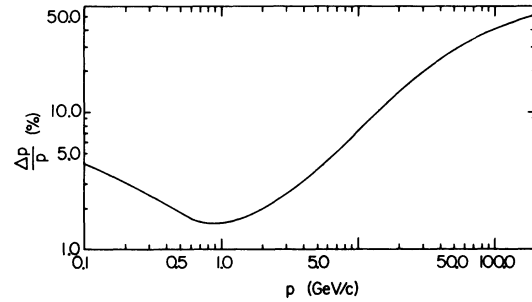


FIG. 1. The momentum-resolution curve for particles with  $\Delta p/p < 0.75$ .

that the fraction of positive pions with  $x > 0.6$  is also 1.3%, and thus we introduce only a small error by assigning the proton mass to all positive particles in that region. The very fast positive particles for which the momentum could not be determined (5% of the total number of positive tracks) were assigned a momentum of 150 GeV/c and a proton mass. (Only 0.9% of the negative tracks were too straight for momentum determination. They were assigned an arbitrary value of  $p_{lab} = 100$  GeV/c.)

The sign of the electric charge of the secondary particles is given by the sense of curvature of the trajectory in the magnetic field. For very fast tracks, for which it was not possible to determine the curvature, the charge was inferred from charge conservation.

No attempt was made to identify  $K$  mesons or antiprotons, which constitute  $\leq 10\%$  of the number of negative particles.<sup>31</sup> However, the single-particle distributions are corrected for the mass misassignment in a statistical way using a Monte Carlo method. Using published kaon and antiproton distributions,<sup>33-47</sup> a Monte Carlo program generates tracks according to their experimentally observed  $p_T$  and  $y$  distributions. The particle's momentum is first calculated using the "true" mass, and then the rapidity (or any other desired variable) is recalculated assuming the pion mass. This procedure simulates the particle misidentification in the real data. We have used ISR results<sup>31</sup> indicating

TABLE II. Resolution in measurement of various kinematic quantities.

Variable Name	Range	Negative particles			Positive particles		
		$y_{lab} < 1.5$	$1.5 < y_{lab} < 4.5$	$y_{lab} > 4.5$	$y_{lab} < 1.5$	$1.5 < y_{lab} < 4.5$	$y_{lab} > 4.5$
$y_{lab}$		0.006	0.02	0.14	0.006	0.02	0.21
$p_T$ (GeV/c)	0.0-0.2	0.003	0.006	0.036	0.004	0.006	0.064
	0.2-0.6	0.006	0.019	0.096	0.007	0.018	0.13
	>0.6	0.014	0.070	0.26	0.016	0.077	0.33
$x$		0.004	0.002	0.049	0.006	0.002	0.080

that the number of positive kaons is 10% of the number of positive pions and that the number of negative kaons (antiprotons) is 8% (2%) of the number of negative pions.<sup>48</sup>

To correct for misidentified protons, we assume that the proton distribution  $d\sigma/dx$  is constant for  $|x| < 0.8$ .<sup>49,50</sup> A Monte Carlo program generates the proton distribution, normalized to the number of observed protons for  $x$  between  $-0.8$  and  $-0.6$ . Then, as in the kaon case, the laboratory momentum is calculated using the proton mass, and any kinematic quantities of interest are recalculated assuming a pion mass.

In addition, a certain fraction of the Dalitz pairs ( $\pi^0 \rightarrow \gamma e^+ e^-$  decays) have unrecognizable electrons or positrons. To correct for this, the Dalitz-pair distribution has been simulated by a Monte Carlo procedure. We have used the Kroll-Wada formula<sup>51</sup> and assumed that the  $\pi^0$  distributions in  $y$  and  $p_T$  have the same shape as the corresponding  $\pi^\pm$  distributions. We also assume that only  $e^+$  and  $e^-$  with momenta less than 150 MeV/c will be identified in the data. The generated higher-momentum tracks are then assigned a pion mass and their rapidity and  $p_T$  are recalculated. For this correction we have used the average number of  $\pi^0$ 's observed for each charged multiplicity.<sup>14</sup>

Once all corrections have been calculated as a function of  $y$  and  $p_T$ , each track is assigned a weight representing the probability that it is a pion [see Fig. 2]. The corrections were found to be insensitive to reasonable variations of the shape of the  $K^+$ ,  $K^-$ ,  $p$ , and  $\bar{p}$  distributions. In all

results presented here an error of  $\pm 25\%$  has been assigned to the uncertainty in the above corrections.

All single-particle distributions presented in the following section are corrected, unless noted otherwise. The distributions of the negative particles are corrected multiplicity by multiplicity. For the positive particles we present inclusive distributions only, because the semi-inclusive proton distributions are not known.

In this paper we also present uncorrected distributions so that it is important to understand how various quantities are affected by mass misidentification. The particle's rapidity is changed by an appreciable amount only if the transverse momentum is less than its mass. For protons and kaons this occurs frequently, as their average transverse momentum is  $\approx 0.4$  GeV/c. The rapidity will change typically by 0.5 to 1.0 units when the heavier particles are called pions; the direction of the change depends on the frame of reference. In the laboratory frame where the target is stationary, mass misidentification results in an increase in the value of  $|y_{lab}|$  such that the bulk of the distribution  $d\sigma/dy_{lab}$  will be shifted toward larger  $y_{lab}$ . However, if the rapidity is directly calculated in the center-of-mass system, as in a colliding-beam experiment, tracks with  $y_{c.m.} < 0$  are shifted to smaller  $y_{c.m.}$ , while those with  $y_{c.m.} > 0$  have their values increased. The net effect is to widen the distribution  $d\sigma/dy_{c.m.}$ , even to cause a dip near  $y_{c.m.} = 0$ . In determining the value of  $x$ , the effect of mass misidentification is to increase  $x$  for those tracks with  $x < 0$  (as much as 0.2 units depending on the magnitude of the transverse momentum), and to leave essentially unchanged those with  $x > 0$ .

### III. SINGLE-PARTICLE DISTRIBUTIONS

Among general features to consider when investigating single-particle distributions, one is the concept of scaling,<sup>1</sup> according to which, at sufficiently high energies, the invariant cross section  $f(\vec{p}) \equiv Ed^3\sigma/dp^3$  becomes independent of the total c.m. energy of the collision, i.e.,

$$\lim_{s \rightarrow \infty} f(x, p_T, s) = g(x, p_T).$$

In short-range-order models, such "Feynman scaling" follows automatically from the basic assumptions. In the kinematic region of small momenta in the rest frame of the beam (target) particle ("fragmentation region"), the function is predicted to be independent of the nature of the target (beam). Away from the fragmentation regions, i.e., in the "central region" of the center-of-mass system, most models of multiparticle production predict an appearance of a "flat top" in the

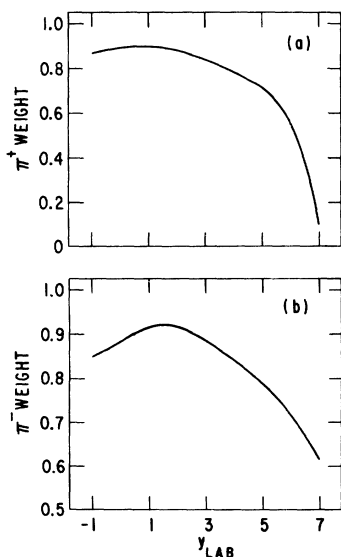


FIG. 2.  $(d\sigma/dy)_{corrected}/(d\sigma/dy)_{uncorrected}$  for (a)  $\pi^+$  and (b)  $\pi^-$ .

rapidity distribution at asymptotic energies,<sup>1</sup> i.e., a cross section in the central region which is independent of both rapidity and the total c.m. energy.

Another interesting question is whether the functional dependence of the invariant cross section on one of the variables (e.g.  $x$  and  $p_T$ ) is independent of the other:

$$g(x, p_T) = g_1(x)g_2(p_T).$$

A simple test of this factorization is to study the average value of  $p_T$  for different  $x$  intervals. If the average value of  $p_T$  should depend on  $x$ , then the cross section does not factorize.

In this section, we examine these points, analyzing single-particle distributions in 205-GeV/c  $pp$  collisions and comparing them with data at other energies.

#### A. Rapidity distributions

In Fig. 3(a) we show the  $\pi^+$  and  $\pi^-$  inclusive rapidity distributions in the laboratory coordinate system.<sup>52</sup> Figure 3(b) gives the ratio of the two cross sections as a function of rapidity:

$$R(\pi^+/\pi^-) = \frac{d\sigma}{dy_{\text{lab}}^{\pi^+}} / \frac{d\sigma}{dy_{\text{lab}}^{\pi^-}}.$$

It is observed that both the  $\pi^+$  and  $\pi^-$  distributions change very little over a central region  $\approx 1.5$  units in rapidity wide. [The insert in Fig. 3(a) shows the  $\pi^-$  central region in finer bins.] Both distributions can be fitted over the range  $1.0 < y_{\text{lab}} < 5.0$  by Gaussians of widths  $2.0 \pm 0.2$  and  $1.5 \pm 0.1$ , respectively (with  $\chi^2$  probabilities of 5% and 15%, respectively).

The ratio of the  $\pi^+$  and  $\pi^-$  cross sections increases from a value of  $\approx 1.15$  near  $90^\circ$  c.m. (Ref. 53) to values greater than 2 in the fragmentation regions. The ISR results indicate that within experimental errors,  $R(\pi^+/\pi^-)$  in the central region is independent of  $s$  over the entire ISR energy range ( $\sqrt{s}$  between 23 and 62 GeV).<sup>41</sup> We therefore compare in Fig. 3(b) our results on  $R(\pi^+/\pi^-)$  with an average of the ISR data<sup>33-47</sup> ( $p_T = 0.4$  GeV/c; solid line). It is seen that our data have a central  $\pi^+/\pi^-$  ratio higher than that observed at ISR. Even if we select only those particles with transverse momenta between 0.3 and 0.5 GeV/c, the ratio remains near 1.15. Our results are consistent with those of other bubble-chamber experiments<sup>54-59</sup> which indicate a decrease of the  $\pi^+/\pi^-$  ratio with increasing energy [from 1.43 at 24 GeV/c (Ref. 56) to 1.15 at 205 GeV/c]. If we assume that the  $90^\circ$  c.m. asymptotic value of the ratio is one, then we conclude that this limit is being approached from above. At 205 GeV/c, effects due to the nature of the beam particle are still noticeable in the central

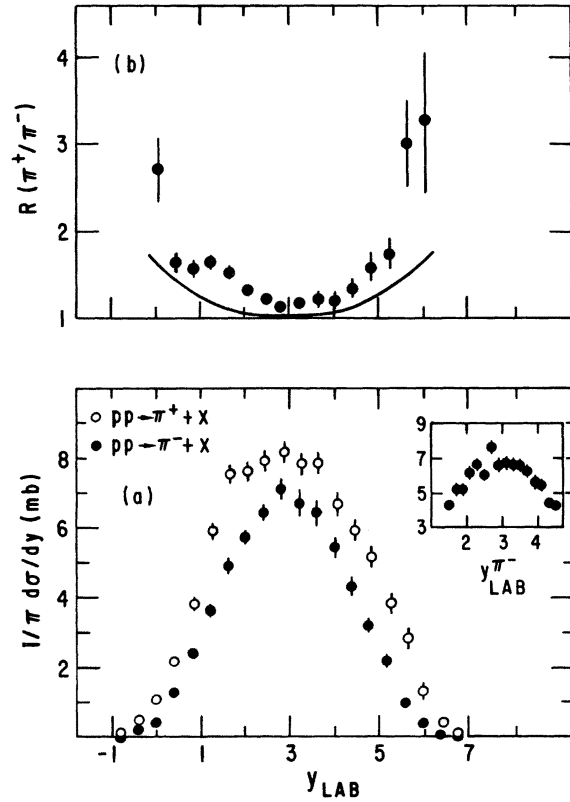


FIG. 3. (a) The single-particle inclusive distributions in laboratory rapidity for  $\pi^+$  (open circles) and  $\pi^-$  (full circles) using a bin size of 0.4 units in rapidity. (Inset: the  $\pi^-$  central region in finer bins.) (b) The ratio of the  $\pi^+$  and the  $\pi^-$  distributions (full circles). The solid curve represents the ISR data at  $p_T = 0.4$  GeV/c (see text).

region.

When we compare the symmetrized inclusive rapidity distributions<sup>60</sup> to the results of other experiments<sup>54-59</sup> in Fig. 4, we observe approximate scaling for  $y_{\text{lab}} < 1.0$ ,<sup>61-63</sup> and a rise of the cross section with increasing c.m. energy for  $y$  in the central region. Thus, if there is scaling in the central region, the asymptotic limit is being approached from below.<sup>61</sup>

The  $\pi^+$  and  $\pi^-$  rapidity distributions for different  $p_T$  intervals are shown in Fig. 5 together with results at 24 GeV/c,<sup>56</sup> as well as at higher energies.<sup>38,41</sup> In the target-fragmentation region, the values of the cross section at different energies are seen to be close to each other, with differences not exceeding 20% on the average. (For the largest  $p_T$  region there are systematic deviations in the  $\pi^+$  case.)

At  $90^\circ$  c.m., the ISR data are consistently above our results only for the lowest  $p_T$  region. For  $p_T > 0.3$  GeV/c, the 205-GeV/c ( $\sqrt{s} = 19.7$ -GeV) data are larger than the  $\sqrt{s} = 23$ -GeV ISR data<sup>41</sup>

(not shown) for both  $\pi^-$  and  $\pi^+$ . The increase of the ISR cross sections with increasing energy then brings the  $\sqrt{s} = 53$ -GeV data<sup>41</sup> close to the 205-GeV/c results (the  $\pi^+$  data for  $p_T \approx 0.8$  GeV/c are an exception). The apparent scaling in the central

region having been reached for larger  $p_T$  at lower energies is best explained as a difference in normalization between the ISR and Fermilab experiments.<sup>64</sup>

Next we study the rapidity distributions for each charged multiplicity separately. Figure 6 shows the semi-inclusive  $\pi^-$  rapidity distributions  $(1/\pi) d\sigma_n/dy_{lab}$ . As the multiplicity increases the widths of the distributions decrease. Only the four-prong events show a flat central rapidity distribution. Table III gives the root-mean-square widths of these distributions,

$$w_n = \frac{1}{N} \left[ \sum_{i=1}^N (y_i - y_{lab}|_{90^\circ \text{ c.m.}})^2 \right]^{1/2},$$

where  $N$  is the number of entries. Only particles with  $y_{lab}$  between 0.4 and 5.6 were included in the calculation of  $w_n$ . The multiplicity dependence of the width  $w_n$  is approximately linear,  $w_n = a + bn_n$ , with  $a = 1.15 \pm 0.01$  and  $b = -0.029 \pm 0.002$ . In addition, the heights of the distributions,  $h_n = (1/\sigma_n) d\sigma_n/dy_{lab}|_{90^\circ \text{ c.m.}}$ , are also given in Table III. The height  $h_n$  increases as the multiplicity increases. A linear fit of the form  $h_n = a + bn_n$  yields  $a = -0.09 \pm 0.02$  and  $b = 2.64 \pm 0.01$ . Similar trends are observed at other energies.<sup>55-57, 102</sup>

As has been noted in Ref. 16, Feynman scaling is not observed in the semi-inclusive rapidity distributions. However, for any given multiplicity, the 205-GeV/c data were found to have values close to those results at other energies which correspond to the same value of the ratio  $n/\langle n \rangle$ .

It has been observed<sup>65, 23</sup> that there is a close connection between the inclusive rapidity distribution at any given  $y$  and the values of the widths of the distributions in charge transfer across  $y$ ,

$$D(y) \equiv \langle u^2(y) \rangle - \langle u(y) \rangle^2.$$

[The charge transfer is defined for each event as

$$u(y) \equiv \frac{1}{2} \times (\text{sum of charges of all particles with } y' > y) - \frac{1}{2} \times (\text{sum of charges of all particles with } y' < y),$$

for beam and target particles of equal charge.] We show in Fig. 7 (see Ref. 66) that a similar relation between  $D_n(y)$  (full circles) and  $\rho_n(y) \equiv (1/\sigma_n) d\sigma_n/dy$  (solid line) is observed for multiplicities  $n > 4$ ,

$$D_n(y) = \alpha_n \rho_n(y).$$

It can be noted that the charge-transfer fluctuations are larger at higher multiplicities [ $D_n(y)$  is increasing with  $n$ ], but the proportionality constant  $\alpha_n$  is decreasing with  $n$ . This can be understood in a cluster picture, if only particles from the "active zone" ( $y - \Delta, y + \Delta$ ) contribute to the charge transfer, and if the length of this interval does not change with multiplicity. (In a cluster picture,  $\Delta$  is solely determined by the properties of the clus-

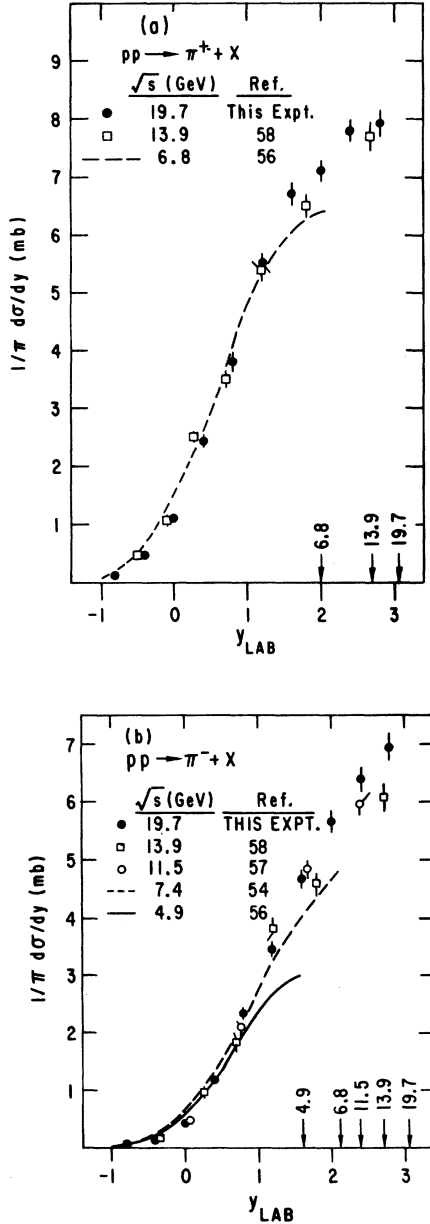


FIG. 4. (a) The single-particle inclusive  $\pi^+$  rapidity distribution at 24 GeV/c (Ref. 56) (dashed line), 102 GeV/c (Ref. 58) (open squares), and 205 GeV/c (full circles). The arrows indicate  $90^\circ$  in the c.m.s. for each c.m. energy. (b) The single-particle inclusive  $\pi^-$  rapidity distribution at 12 GeV/c (Ref. 56) (solid line), 28.5 GeV/c (Ref. 54) (dashed line), 69 GeV/c (Ref. 57) (open circles), 102 GeV/c (Ref. 58) (open squares), and 205 GeV/c (full circles).

ters.) Since the single-particle distributions are narrower for higher multiplicities, a relatively smaller fraction of particles takes part in the charge transfer.

### B. Transverse-momentum distributions

The  $\pi^+$  and  $\pi^-$  inclusive distributions in transverse momentum squared,  $p_T^2$ , are shown in Fig. 8. It is obvious that a single exponential in  $p_T^2$  will not fit the data since a change in slope occurs near  $p_T^2 = 0.2$  (GeV/c)<sup>2</sup>. A sum of two Gaussian functions of the form  $d\sigma/dp_T^2 = A \exp(-Bp_T^2) + C \exp(-Dp_T^2)$  yields a good fit over the whole  $p_T$  interval, while single Gaussian functions fit the data in the regions below and above  $p_T^2 = 0.2$  (GeV/c)<sup>2</sup> separately. Tables IV(a) and IV(b) summarize the results.

The change in slope also occurs for the semi-inclusive distributions  $d\sigma_n/dp_T^2$ , so that the slope change in the inclusive distribution is not a result

of combining different multiplicities. For  $p_T^2 < 0.2$  (GeV/c)<sup>2</sup>, the data for the lower multiplicities tend to have a smaller slope, while for  $p_T^2 > 0.2$  (GeV/c)<sup>2</sup>, the slope is consistent with being independent of multiplicity. (See Tables V and VI for parametrizations of  $d\sigma_n/dp_T^2$ .)

Results at other energies shown in Fig. 8 by the solid line [28.5 GeV/c (Ref. 54)] and by the dashed line [102 GeV/c (Ref. 58)] exhibit a similar  $p_T^2$  dependence as the 205-GeV/c data. The increase in  $d\sigma/dp_T^2$  with energy is mainly a reflection of the increase in the average multiplicity.

The invariant  $p_T^2$  distributions for various  $x$  intervals are shown in Fig. 9. For  $|x| < 0.01$ ,  $Ed^3\sigma/dp^3$  in the low- $p_T^2$  region decreases sharply with increasing  $p_T^2$ , and a break near  $p_T^2 = 0.2$  (GeV/c)<sup>2</sup> is observed. For  $0.04 < |x| < 0.1$ , the slope for  $p_T^2 < 0.2$  (GeV/c)<sup>2</sup> is less than the corresponding slope for the smaller  $x$  region. For  $0.1 < |x| < 0.2$ , the cross section is consistent with being constant for  $p_T^2 < 0.08$  (GeV/c)<sup>2</sup>. (This effect

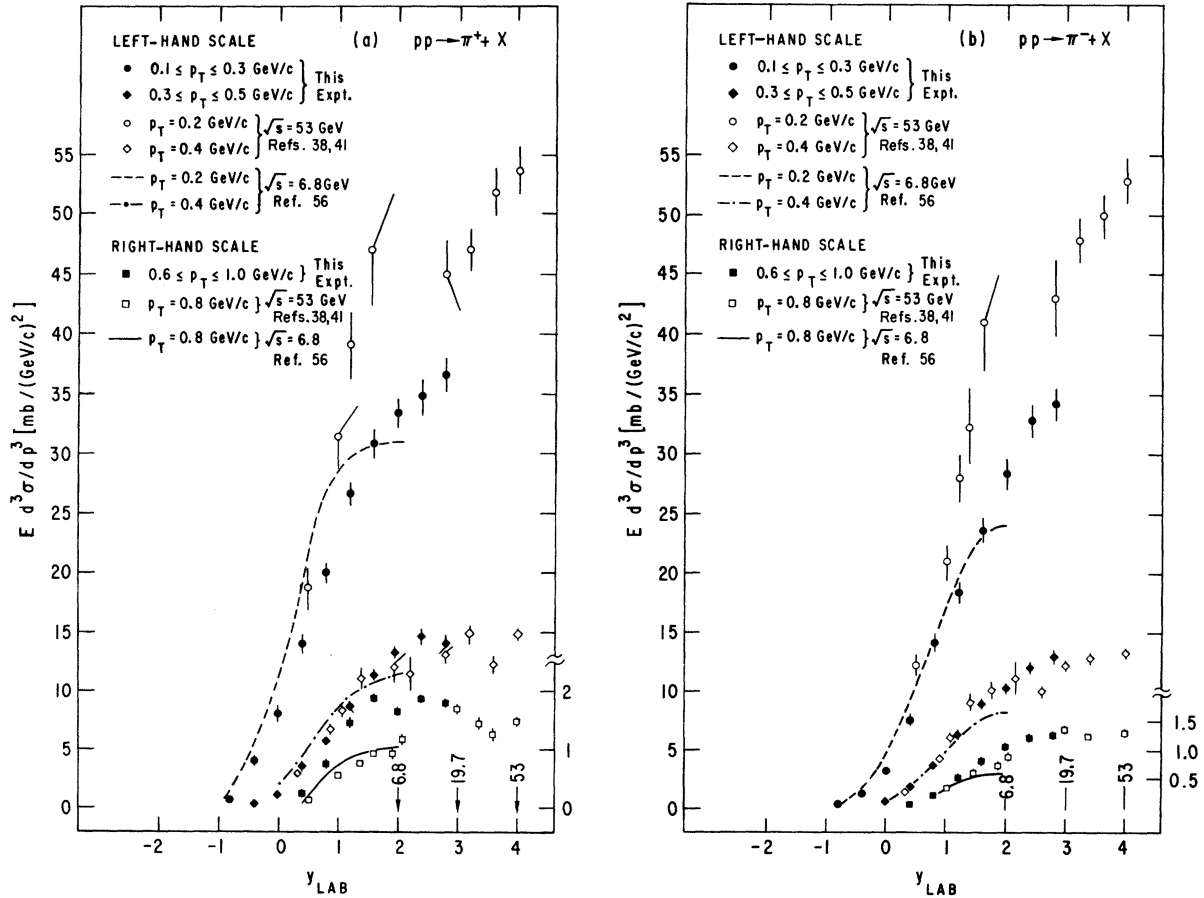


FIG. 5. (a) The single-particle inclusive  $\pi^+$  rapidity distributions for three values of  $p_T$ . (The ISR values are for  $\sqrt{s} = 53$  GeV except for the points below  $y_{\text{lab}} = 0.6$  which are for  $\sqrt{s} = 30.6$  GeV. The data for  $y_{\text{lab}} > 2.5$  are from Ref. 41, for  $y_{\text{lab}} < 2.5$  from Ref. 38.) The arrows indicate  $90^\circ$  in the c.m.s. for each c.m. energy. (b) The single-particle inclusive  $\pi^-$  rapidity distributions for three values of  $p_T$ .

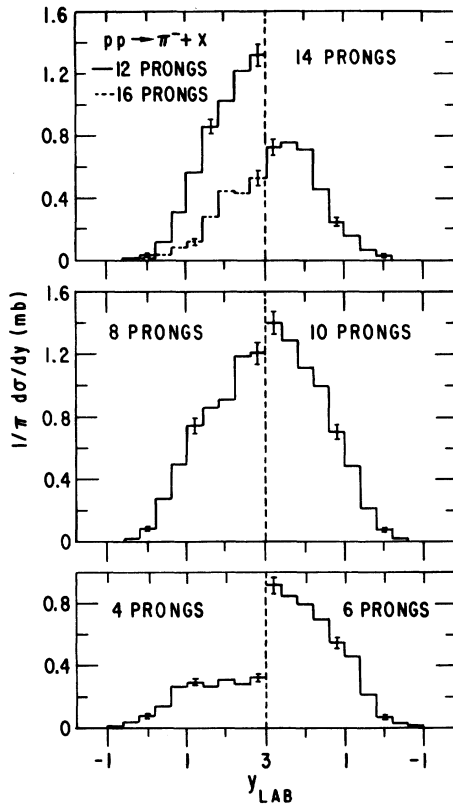


FIG. 6. Semi-inclusive rapidity distributions for negative pions.

is not caused by poor resolution due to inadequate momentum measurement of fast particles, since the same  $p_T$  dependence is observed when only particles with  $x < 0$  are included in the distributions.) As  $p_T^2$  increases, the difference between the slopes of the distributions in individual  $x$  intervals decreases.

As in the case of the  $p_T^2$  distribution integrated over all  $x$ , a single exponential in  $p_T$  or  $p_T^2$  does not fit the  $90^\circ$  c.m. data, but the sum of two exponentials in  $p_T^2$  does represent it fairly well.

TABLE III. The widths and heights of the  $\pi^+$  and  $\pi^-$  inclusive and semi-inclusive rapidity distributions for  $0.4 \leq y_{\text{lab}} \leq 5.6$ .

Multiplicity	Particle	$w_n$	$\frac{1}{\sigma_n} \frac{d\sigma_n}{dy} \Big _{90^\circ \text{ c.m.}}$
4	$\pi^-$	$1.135 \pm 0.025$	$0.18 \pm 0.02$
6	$\pi^-$	$1.070 \pm 0.040$	$0.42 \pm 0.03$
8	$\pi^-$	$1.054 \pm 0.012$	$0.66 \pm 0.05$
10	$\pi^-$	$1.035 \pm 0.011$	$1.01 \pm 0.07$
12	$\pi^-$	$1.008 \pm 0.011$	$1.28 \pm 0.10$
14	$\pi^-$	$0.973 \pm 0.014$	$1.46 \pm 0.14$
16	$\pi^-$	$0.945 \pm 0.018$	$1.97 \pm 0.26$
Inclusive	$\pi^+$	$1.048 \pm 0.004$	$0.78 \pm 0.03$
Inclusive	$\pi^-$	$1.025 \pm 0.005$	$0.68 \pm 0.03$

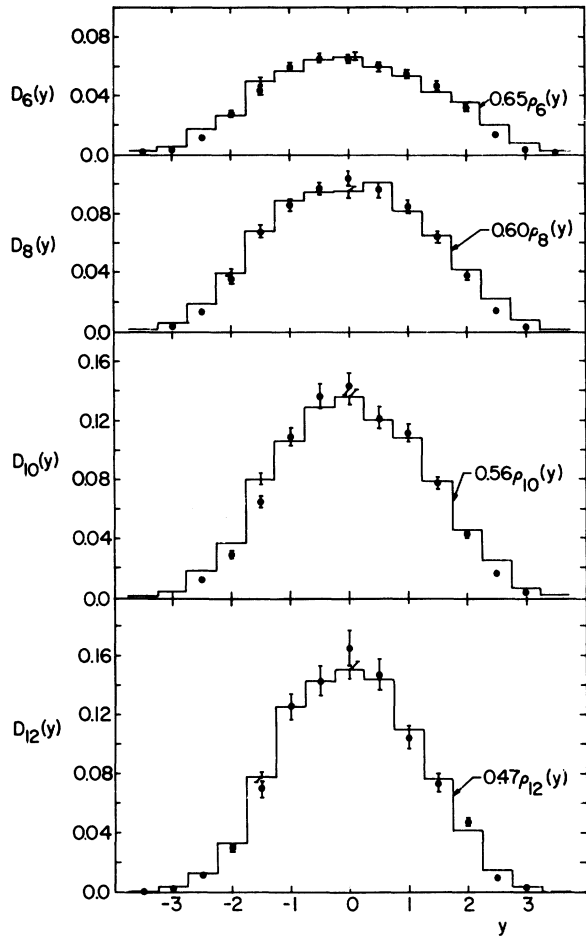


FIG. 7. The dispersion of the semi-inclusive charge transfer distributions,  $D_n(y)$ , as a function of c.m. rapidity for 6-, 8-, 10-, and 12-prong events (full circles). The solid curves represent the semi-inclusive single-particle densities (multiplied by a constant, as indicated).

Table VII gives parameters for fits to the data for  $|x| \leq 0.02$ . In addition, the form  $A \exp(-Bp_T + Cp_T^2)$  also fits the data. However, the particular values of the parameters obtained by the Saclay-Strasbourg collaboration (SS) at ISR (Ref. 33) for the latter fit give poor results when applied to our data, as the ISR results suggest much larger values of the cross section at small  $p_T$ . Results similar to those of the SS collaboration have been found by the British-Scandinavian collaboration (BS) (Refs. 40 and 41) in an ISR experiment extending the  $p_T$  region down to  $\approx 0.03$  GeV/c. However, other bubble-chamber experiments which cover the beam momentum range between 12 and 100 GeV/c (Refs. 54-59) find results similar to ours.

We have attempted to fit the  $90^\circ$  c.m.  $p_T^2$  distributions to other forms (see Table VII):  $A \exp(-B\mu)$  (Ref. 67) (where  $\mu = (p_T^2 + m^2)^{1/2}$ , the longitudinal mass), Hagedorn's thermodynamic formula<sup>68</sup>

$AE[\exp(B\mu + C)]^{-1}$  (where  $E$  is the particle's c.m. energy and  $C = -1, 0, \text{ or } +1$ ), and Landau's hydrodynamical model,<sup>69</sup>  $A \exp(-By_T^2)$ , where  $y_T \equiv \frac{1}{2} \ln[(E + p_T)/(E - p_T)]$ . The thermodynamic model fits the data well when  $C = -1$  (this is the proper choice of  $C$  for identical bosons). Over the whole  $p_T$  range, the hydrodynamic model does not fit very well. However, for  $p_T^2 > 0.2 \text{ (GeV/c)}^2$ , i.e., in the region where the model is expected to apply better, we obtain a reasonable fit. The exponential in the longitudinal mass is also an acceptable parametrization.

The dependence of the transverse-momentum distribution on the charged multiplicity and on the longitudinal variables,  $x$  and  $y$ , as well as on the radial-scaling variable,  $x_R \equiv 2E_{c.m.}/\sqrt{s}$ , is illustrated in Figs. 10 through 14, where the average value of the transverse momentum is displayed as a function of the respective variable.<sup>70</sup> [The overall averages are  $\langle p_T^* \rangle = (0.336 \pm 0.003) \text{ GeV/c}$ ,  $\langle p_T^* \rangle = (0.373 \pm 0.002) \text{ GeV/c}$ ,  $\langle (p_T^*)^2 \rangle = (0.161 \pm 0.003) \text{ (GeV/c)}^2$ ,  $\langle (p_T^*)^2 \rangle = (0.199 \pm 0.003) \text{ (GeV/c)}^2$ .]

A decrease in  $\langle p_T \rangle_n$  as the multiplicity increases is observed for both  $\pi^+$  and  $\pi^-$  (Fig. 10). In fact, the data can be fitted by straight lines,  $\langle p_T^* \rangle_n = a_1 + b_1 n_-$  and  $\langle p_T^* \rangle_n = a_2 + b_2 n_+$ , with  $a_1 = 0.375 \pm 0.007$ ,  $b_1 = -0.0098 \pm 0.0006$ ,  $a_2 = 0.395 \pm 0.008$ , and  $b_2 = -0.006 \pm 0.001$ . Figure 11 shows the  $x$  dependence of  $\langle p_T^* \rangle_x$  [Fig. 11(a)] and  $\langle p_T^* \rangle_x$  [Fig. 11(b)]. We observe that  $\langle p_T \rangle_x$  increases as  $|x|$  is increased, the well-known sea-gull effect.<sup>71</sup> A similar sharp increase of the average transverse momentum is observed in its  $x_R$  dependence (Fig. 12) for  $|x_R| < 0.1$ ; for larger  $|x_R|$ , the change of  $\langle p_T \rangle_{x_R}$  with increasing  $|x_R|$  is smaller than in the case of  $\langle p_T \rangle_x$ . Figure 13 exhibits  $\langle p_T^* \rangle_y$  and  $\langle p_T^* \rangle_y$  versus

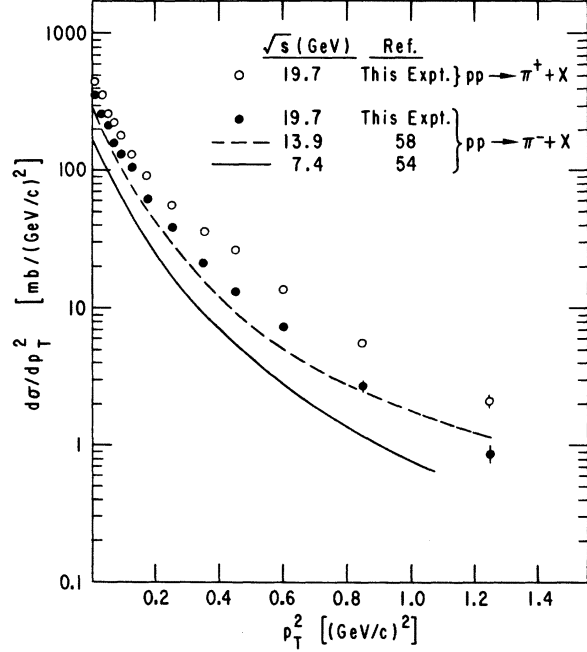


FIG. 8. The single-particle inclusive distributions in the square of the transverse-momentum magnitude,  $p_T^2$ , for both positive pions (open circles) and negative pions (full circles). Lower-energy  $\pi^-$  data are shown by the solid line [28.5 GeV/c (Ref. 54)] and by the dashed line [102 GeV/c (Ref. 58)].

$y_{lab}$ . A decrease in  $\langle p_T \rangle_y$  is observed for  $y$  away from the central region. (A decrease toward the edge of phase space is expected from energy and momentum conservation.) In addition,  $\langle p_T \rangle_y$  is consistent with being constant for  $1 < y_{lab} < 5$ .

A brief look at the multiplicity dependence of the sea-gull effect in the case of the  $x$  dependence of

TABLE IV. Results of various fits to the inclusive  $p_T^2$  distributions for (a)  $\pi^+$  and (b)  $\pi^-$ .

Form	$p_T^2$ interval [(GeV/c) <sup>2</sup> ]	Fitted parameters		$\chi^2/\text{DOF}$
(a) $\pi^+$				
$A \exp(-Bp_T^2)$	0.0–0.7	$A = (394 \pm 20) \text{ mb (GeV/c)}^{-2}$	$B = (14.7 \pm 0.6) \text{ (GeV/c)}^{-2}$	5.6/7
$+ C \exp(-Dp_T^2)$		$C = (98 \pm 3) \text{ mb (GeV/c)}^{-2}$	$D = (3.2 \pm 0.1) \text{ (GeV/c)}^{-2}$	
$A \exp(-Bp_T^2)$	0.0–0.7			155/7
$A \exp(-Bp_T^2)$	0.0–0.2	$A = (450 \pm 5) \text{ mb (GeV/c)}^{-2}$	$B = (9.7 \pm 0.4) \text{ (GeV/c)}^{-2}$	9.4/5
$A \exp(-Bp_T^2)$	0.2–0.7	$A = (144 \pm 1) \text{ mb (GeV/c)}^{-2}$	$B = (3.9 \pm 0.1) \text{ (GeV/c)}^{-2}$	1.5/3
(b) $\pi^-$				
$A \exp(-Bp_T^2)$	0.0–0.7	$A = (304 \pm 23) \text{ mb (GeV/c)}^{-2}$	$B = (14.6 \pm 0.3) \text{ (GeV/c)}^{-2}$	6.1/7
$+ C \exp(-Dp_T^2)$		$C = (80 \pm 11) \text{ mb (GeV/c)}^{-2}$	$D = (4.0 \pm 0.3) \text{ (GeV/c)}^{-2}$	
$A \exp(-Bp_T^2)$	0.0–0.7			181/7
$A \exp(-Bp_T^2)$	0.0–0.2	$A = (360 \pm 17) \text{ mb (GeV/c)}^{-2}$	$B = (10.2 \pm 0.4) \text{ (GeV/c)}^{-2}$	7.9/5
$A \exp(-Bp_T^2)$	0.2–0.7	$A = (106 \pm 15) \text{ mb (GeV/c)}^{-2}$	$B = (4.5 \pm 0.3) \text{ (GeV/c)}^{-2}$	6.7/3

TABLE V. Results of the fit  $A \exp(-B p_T^2) + C \exp(-D p_T^2)$  to the semi-inclusive  $\pi^- p_T^2$  distributions for  $p_T^2 < 0.7$  (GeV/c)<sup>2</sup>.

Multiplicity	A [ $\frac{\text{mb}}{(\text{GeV}/c)^2}$ ]	B [(GeV/c) <sup>-2</sup> ]	C [ $\frac{\text{mb}}{(\text{GeV}/c)^2}$ ]	D [(GeV/c) <sup>-2</sup> ]	$\chi^2/\text{DOF}$
4	16 ± 2	10.4 ± 1.9	4 ± 1	3.4 ± 0.6	6.3/7
6	41 ± 1	12.1 ± 0.3	10 ± 1	3.5 ± 0.1	4.8/7
8	56 ± 4	12.7 ± 0.9	10 ± 1	3.0 ± 0.6	17.3/7
10	57 ± 11	11.9 ± 0.7	13 ± 6	3.9 ± 0.8	2.2/7
12	66 ± 4	12.6 ± 0.5	7 ± 3	3.3 ± 0.8	11.5/7
14	37 ± 6	14.1 ± 2.3	4 ± 1	2.6 ± 0.3	18.1/7
16	30 ± 2	19.3 ± 1.0	4 ± 1	4.3 ± 0.1	8.8/7

the  $\pi^-$  average transverse momentum (Fig. 14) suggests that the central dip in  $\langle p_T^* \rangle_x$  is more pronounced in events with higher multiplicity.

From the examination of the dependence of  $\langle p_T \rangle_a$  on the longitudinal momentum variables ( $a=x, y$ ) and on the radial variable  $x_R$  we conclude that the single-particle inclusive distributions do not factorize either in  $x$  in  $p_T$ , in  $y$  and  $p_T$ , or in  $x_R$  and  $p_T$ . The same conclusions also hold for the semi-inclusive distributions.

Another fact stands out in all the above results. Consistently,  $\langle p_T^* \rangle$  is greater than  $\langle p_T^* \rangle_x$ , i.e., the shape (as well as the magnitude) of the  $\pi^+$  and  $\pi^- p_T$  distributions are different. It can also be seen in Tables IV (a) and IV (b) that the slopes of the  $p_T^2$  distributions are always larger for  $\pi^-$  than for  $\pi^+$ . Figure 15, which gives the ratio

$$R(\pi^+/\pi^-) = \frac{d\sigma}{d(p_T^*)^2} \bigg/ \frac{d\sigma}{d(p_T^*)^2}$$

as a function of  $p_T^2$ , shows this effect more dramatically. There is a clear trend in the data (not explainable by proton contamination) for the ratio to rise with increasing  $p_T^2$ . This rise occurs in all  $x$  intervals. In fact, independent of  $x$  we find

$$\frac{R(\pi^+/\pi^-)|_{p_T^2 > 0.2 (\text{GeV}/c)^2}}{R(\pi^+/\pi^-)|_{p_T^2 < 0.2 (\text{GeV}/c)^2}} \approx 1.4.$$

### C. The $x$ distributions

In Fig. 16 we give the invariant  $x$  distributions for  $\pi^+$  and  $\pi^-$  integrated over all  $p_T$ . Curves representing 24-GeV/c  $pp$  results<sup>56</sup> are also shown. As in the rapidity distributions, we observe approximate scaling in the fragmentation region,  $|x| > 0.2$ . The slope of the distribution for  $|x| < 0.2$  is smaller than for  $|x| > 0.2$ , with a hint of a region of constant invariant cross section near  $x=0$ . The distributions can be parametrized in the form  $A \exp(-B|x|)$ . For  $|x| > 0.02$ , results of various fits to the inclusive  $x$  distributions are given in Table VIII. In fact, in the  $\pi^-$  case, a good fit is obtained over the whole  $x$  range. A suitable pa-

rametrization of both distributions over the whole  $x$  range has the form  $A \exp(-B|x| + C|x|^2)$ .

Semi-inclusive  $\pi^- x$  distributions (not shown) can also be parametrized by the exponential function. Table IX gives the results of fits of the form  $A \exp(-B|x|)$  to the invariant distributions  $(2E/\pi\sqrt{s}) d\sigma_n/dx$  in the interval  $0.02 < |x| < 0.4$  as a function of multiplicity. Note that as the multiplicity increases, the value of  $B$  increases.

The invariant  $x$  distribution for various intervals of transverse momentum is plotted in Fig. 17 along with data from experiments performed at other energies. We observe that for  $|x| > 0.1$ , the data are equal within errors to the ISR results except for the case of  $0.6 < p_T^* < 1.0$  GeV/c. (This discrepancy was noted previously in the rapidity distributions, as well as in connection with the transverse-momentum dependence of the  $\pi^+/\pi^-$  ratio.) Note that as  $p_T$  increases, the length of the flat part near  $x=0$  increases. The slopes are consistent with being the same for  $|x| > 0.15$ .

## IV. TWO-PARTICLE CORRELATIONS

### A. The correlation functions

We next investigate two-particle distributions, obtained from the full differential cross sections by integrating over variables describing all particles but the two of interest. To determine how the

TABLE VI. Results of the fit  $A \exp(-B p_T^2)$  to the semi-inclusive  $\pi^- p_T^2$  distributions for  $p_T^2 < 0.2$  (GeV/c)<sup>2</sup>.

Multiplicity	A [ $\frac{\text{mb}}{(\text{GeV}/c)^2}$ ]	B [(GeV/c) <sup>-2</sup> ]	$\chi^2/\text{DOF}$
4	18 ± 4	8.9 ± 2.0	5.3/5
6	49 ± 6	9.9 ± 1.1	2.8/5
8	62 ± 1	10.2 ± 0.6	13.6/5
10	69 ± 1	9.8 ± 0.7	2.2/5
12	75 ± 4	12.0 ± 1.2	6.1/5
14	39 ± 2	12.2 ± 0.4	14.1/5
16	33 ± 3	17.3 ± 3.5	2.3/5

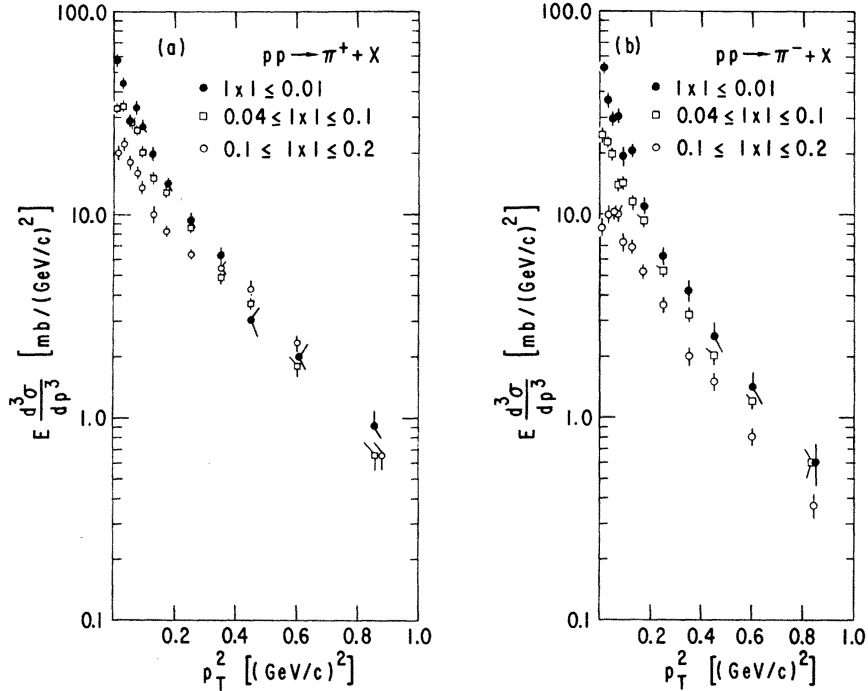


FIG. 9. The single-particle inclusive  $p_T^2$  distributions for the production of (a) positive and (b) negative pions in three  $x$  intervals:  $|x| \leq 0.01$  (full circles),  $0.04 \leq |x| \leq 0.1$  (open squares), and  $0.1 \leq |x| \leq 0.2$  (open circles).

TABLE VII. Results of various fits to the  $p_T^2$  dependence of the 90° c.m. values of the invariant cross section in the interval  $p_T^2 < 0.7$  (GeV/c)<sup>2</sup> for (a)  $\pi^+$  and (b)  $\pi^-$ .

Form	Fitted parameters		$\chi^2/\text{DOF}$
(a) $\pi^+$			
$A \exp(-B p_T^2)$	$A = (45 \pm 4) \text{ mb (GeV/c)}^{-2}$	$B = (11.4 \pm 0.9) \text{ (GeV/c)}^{-2}$	4.3/7
$+ C \exp(-D p_T^2)$	$C = (11 \pm 1) \text{ mb (GeV/c)}^{-2}$	$D = (2.9 \pm 0.2) \text{ (GeV/c)}^{-2}$	
$A \exp(-B p_T + C p_T^2)$	$A = (83 \pm 11) \text{ mb (GeV/c)}^{-2}$	$B = (3.6 \pm 0.7) \text{ (GeV/c)}^{-1}$	7.3/8
		$C = (-1.7 \pm 0.7) \text{ (GeV/c)}^{-2}$	
$A \exp(-B\mu)$	$A = (143 \pm 2) \text{ mb (GeV/c)}^{-2}$	$B = (5.5 \pm 0.1) \text{ GeV}^{-1}$	5.9/9
$AE [\exp(B\mu) - 1]^{-1}$	$A = (693 \pm 90) \text{ mb GeV}^{-1} c^2$	$B = (7.3 \pm 0.2) \text{ GeV}^{-1}$	6.2/9
$AE [\exp(B\mu)]^{-1}$	$A = (969 \pm 60) \text{ mb GeV}^{-1} c^2$	$B = (7.9 \pm 0.1) \text{ GeV}^{-1}$	10.2/9
$AE [\exp(B\mu) + 1]^{-1}$	$A = (1205 \pm 30) \text{ mb GeV}^{-1} c^2$	$B = (8.2 \pm 0.1) \text{ GeV}^{-1}$	18.1/9
$A \exp(-B y_T^2)$	$A = (76 \pm 1) \text{ mb (GeV/c)}^{-2}$	$B = 0.71 \pm 0.02$	24.5/9
(b) $\pi^-$			
$A \exp(-B p_T^2)$	$A = (44 \pm 2) \text{ mb (GeV/c)}^{-2}$	$B = (13.3 \pm 0.1) \text{ (GeV/c)}^{-2}$	11.4/7
$+ C \exp(-D p_T^2)$	$C = (12 \pm 3) \text{ mb (GeV/c)}^{-2}$	$D = (3.6 \pm 0.4) \text{ (GeV/c)}^{-2}$	
$A \exp(-B p_T + C p_T^2)$	$A = (79 \pm 10) \text{ mb (GeV/c)}^{-2}$	$B = (3.8 \pm 0.9) \text{ (GeV/c)}^{-1}$	13.1/8
		$C = (-2.1 \pm 1.2) \text{ (GeV/c)}^{-2}$	
$A \exp(-B\mu)$	$A = (146 \pm 11) \text{ mb (GeV/c)}^{-2}$	$B = (6.0 \pm 0.1) \text{ GeV}^{-1}$	12.5/9
$AE [\exp(B\mu) - 1]^{-1}$	$A = (751 \pm 41) \text{ mb GeV}^{-1} c^2$	$B = (7.9 \pm 0.2) \text{ GeV}^{-1}$	11.9/9
$AE [\exp(B\mu)]^{-1}$	$A = (1081 \pm 50) \text{ mb GeV}^{-1} c^2$	$B = (8.6 \pm 0.2) \text{ GeV}^{-1}$	15.1/9
$AE [\exp(B\mu) + 1]^{-1}$	$A = (1370 \pm 69) \text{ mb GeV}^{-1} c^2$	$B = (9.0 \pm 0.2) \text{ GeV}^{-1}$	22.5/9
$A \exp(-B y_T^2)$	$A = (70 \pm 3) \text{ mb (GeV/c)}^{-2}$	$B = 0.75 \pm 0.03$	31.0/9

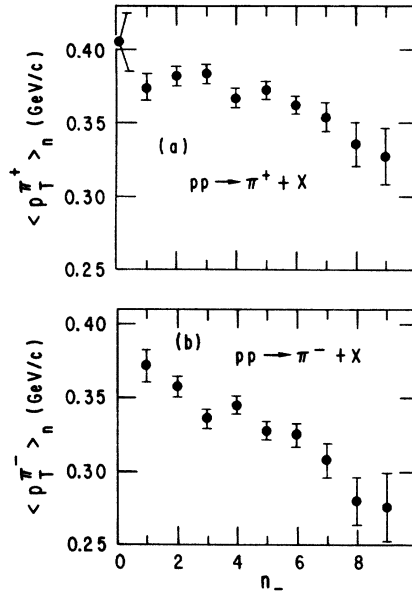


FIG. 10. The multiplicity dependence of the average transverse momentum of (a) positive pions and (b) negative pions.

production of a pair of particles differs from the case when each particle is produced independently, the two-particle distributions are compared with a suitable combination of single-particle distributions.

In ensembles of atoms and molecules, the inter-

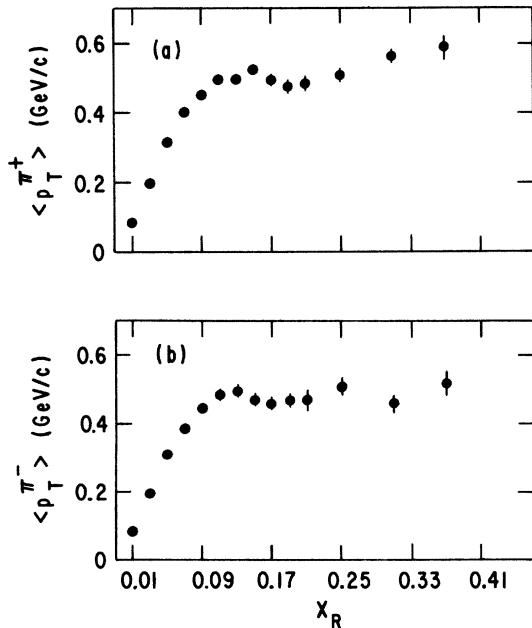


FIG. 12. The  $x_R$  dependence of the average transverse momentum of (a) positive pions and (b) negative pions.

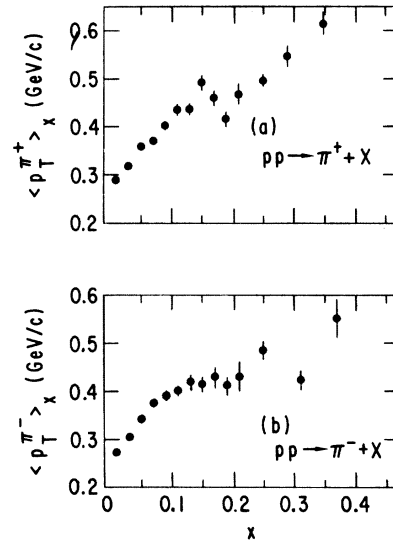


FIG. 11. The  $x$  dependence of the average transverse momentum of (a) positive pions and (b) negative pions. (The bin size is  $\Delta x = 0.04$ .)

dependence in position of the particles has been described using correlation functions. By analogy, correlation functions in momentum space were introduced by Mueller<sup>72</sup> and Wilson<sup>73</sup> as a tool for investigating multiparticle production in high-energy hadron collisions. These functions can be written, in general, as

$$C(\vec{p}_1, \vec{p}_2) \equiv \frac{1}{\sigma} \frac{d\sigma}{d\vec{p}_1 d\vec{p}_2} - \frac{1}{\sigma} \frac{d\sigma}{d\vec{p}_1} \frac{1}{\sigma} \frac{d\sigma}{d\vec{p}_2}. \quad (1)$$

After integration over transverse momenta, one can write the inclusive correlation function using

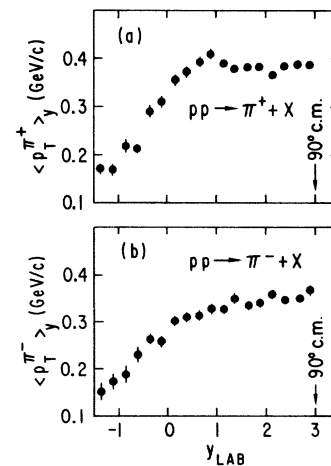


FIG. 13. The rapidity dependence of the average transverse momentum of (a) positive pions and (b) negative pions. (The bin size is  $\Delta y = 0.25$ .)

rapidity as the independent variable:

$$C^{\alpha\beta}(y_1^\alpha, y_2^\beta) \equiv \rho^{\alpha\beta}(y_1^\alpha, y_2^\beta) - \rho^\alpha(y_1^\alpha)\rho^\beta(y_2^\beta), \quad (2)$$

where  $\rho^\alpha(y^\alpha) \equiv (1/\sigma)d\sigma/dy^\alpha$  and  $\rho^{\alpha\beta}(y_1^\alpha, y_2^\beta) \equiv (1/\sigma)d^2\sigma/dy_1^\alpha dy_2^\beta$  are the one- and two-particle inclusive rapidity distributions, and  $\sigma$  is the inelastic cross section. (The superscripts  $\alpha$  and  $\beta$  are used to label the charge combination, as defined in Sec. I.) Often a "normalized" correlation function

$$R(y_1, y_2) \equiv \frac{C(y_1, y_2)}{\rho(y_1)\rho(y_2)}$$

is introduced for experimental reasons, e.g., to avoid difficulties with cross-section normalization.<sup>74</sup>

Results on the correlation functions are presented in this section and in Sec. V using the center-of-mass rapidity,  $y$ , as the independent variable. All distributions in Secs. IV A through IV C and in Sec. V are integrated over the transverse momenta of the particles and all distributions are symmetrized about  $y=0$ . The errors on the values of the correlation functions are statistical only and take into account the fact that the one- and two-particle distributions are not statistically independent quantities. Unless otherwise noted, all distributions displayed here were obtained using a bin size of 0.5 units in rapidity.

Values of  $R(y_1, y_2)$  for the  $cc$  combination are shown in Fig. 18, where curves of  $R^{cc}(y_1, y_2) = \text{const}$  are drawn in the  $(y_1, y_2)$  plane.<sup>75</sup> The two-fold symmetry of the plot with respect to the lines  $y_1 - y_2 = \text{const}$  and  $y_1 + y_2 = \text{const}$ <sup>76</sup> has been exploited in the presentation of our data: All one-dimension-

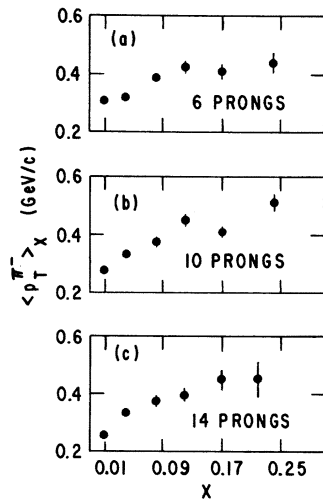


FIG. 14. The  $x$  dependence of the average  $\pi^-$  transverse momentum for three semi-inclusive data samples: (a) 6-prong events (b) 10-prong events, and (c) 14-prong events.

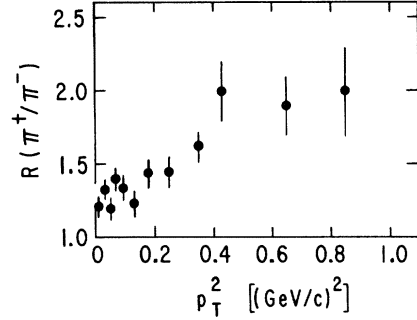


FIG. 15. The ratio of the  $p_T^2$  distributions for the positive and for the negative pions.

al plots shown in this section represent a cut of the two-dimensional distributions along one of these two directions.

The elongation of the contour lines in the direction  $y_1 + y_2 = \text{const}$  shows that  $R(y_1, y_2)$  depends in the central region on  $|y_1 - y_2|$  only, a property called "translational invariance" in rapidity.

Another view of this feature is shown in Fig. 19, where both  $C(y_1, y_2)$  and  $R(y_1, y_2)$  are plotted as a function of  $\frac{1}{2}(y_1 + y_2)$  for a fixed value of  $\frac{1}{2}(y_1 - y_2) = 0$ . The  $C$  function decreases by 32% over 1 unit of rapidity. On the other hand, the  $R$  function decreases by 9% over the same interval, thus showing an approximate  $(y_1 + y_2)$  independence, as seen

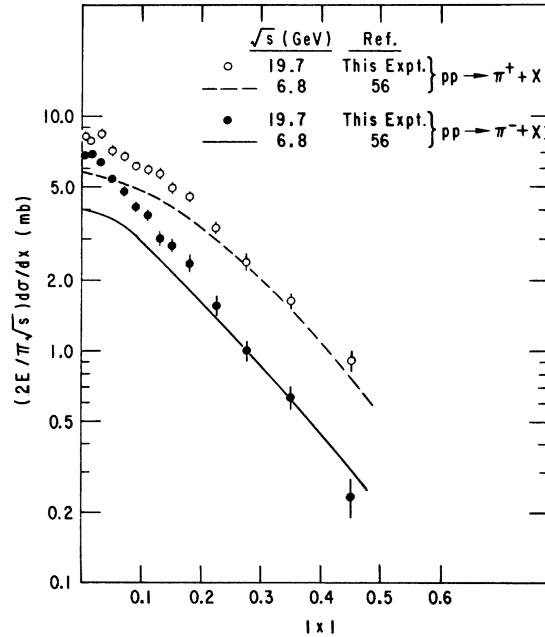


FIG. 16. The single-particle inclusive  $x$  distributions for the positive pions (open circles) and for the negative pions (full circles). The 24-GeV/c data (Ref. 56) for the production of positive (negative) pions are shown by the dashed (solid) line.

TABLE VIII. Results of various fits to the inclusive  $x$  distributions.

Form	Particle	$x$ interval	Fitted parameters		$\chi^2/\text{DOF}$
$A \exp(-B x )$	$\pi^-$	$ x  > 0.02$	$A = (8.0 \pm 0.3) \text{ mb}$	$B = 7.4 \pm 0.1$	6.6/10
	$\pi^-$	all $x$	$A = (7.7 \pm 0.2) \text{ mb}$	$B = 7.2 \pm 0.4$	12.3/12
	$\pi^+$	$ x  > 0.02$	$A = (10.0 \pm 0.1) \text{ mb}$	$B = 5.0 \pm 0.1$	17.7/10
$A \exp(-B x  + C x ^2)$	$\pi^-$	all $x$	$A = (7.3 \pm 0.2) \text{ mb}$ $C = 3.9 \pm 0.5$	$B = 5.8 \pm 0.1$	4.8/11
	$\pi^+$	all $x$	$A = (8.5 \pm 0.2) \text{ mb}$ $C = 5.1 \pm 0.8$	$B = 2.9 \pm 0.1$	8.3/11

already in Fig. 18. The reason for this difference lies in the fact that the shape of the single-particle rapidity distribution,  $\rho(y)$ , is similar to the shape of  $C(y_1, y_2)$  (cf. Fig. 3). Since  $R(y_1, y_2)$  reflects the shape of  $C(y_1, y_2)$  only if  $\rho(y) = \text{const}$ , in the following discussion we will use only the  $C$  functions.

A correlation function can also be defined for a data sample containing events with given charged multiplicity  $n$  ("semi-inclusive correlation function"):

$$C_n^{\alpha\beta}(y_1^\alpha, y_2^\beta) \equiv \rho_n^{\alpha\beta}(y_1^\alpha, y_2^\beta) - \rho_n^\alpha(y_1^\alpha) \rho_n^\beta(y_2^\beta), \quad (3)$$

where  $\rho_n^\alpha(y^\alpha) \equiv (1/\sigma_n) d\sigma_n/dy^\alpha$  and  $\rho_n^{\alpha\beta}(y_1^\alpha, y_2^\beta) \equiv (1/\sigma_n) d^2\sigma_n/dy_1^\alpha dy_2^\beta$  are the one- and two-particle semi-inclusive rapidity distributions, and  $\sigma_n$  is the topological cross section. Note that the distributions are normalized in such a way that  $\int \rho_n^\alpha(y^\alpha) dy^\alpha = n(\alpha)$ , the number of particles of type  $\alpha$  in an event with charged multiplicity  $n$ , and

$$\int \rho_n^{\alpha\beta}(y_1^\alpha, y_2^\beta) dy_1^\alpha dy_2^\beta = n(\alpha\beta) \equiv n(\alpha)n(\beta) - n(\alpha)\delta_{\alpha\beta}, \quad (2)$$

the number of two-particle combinations in which one particle is of type  $\alpha$  and the other is of type  $\beta$ , again in an event with charged multiplicity  $n$ . Note that the condition  $C_n^{\alpha\beta}(y_1^\alpha, y_2^\beta) = 0$  does not describe a sample in which particles are emitted statistically uncorrelated.

Following Ref. 77, we use the notion of the probability of the simultaneous occurrence of two independent phenomena to obtain a more suitable def-

inition of the semi-inclusive correlation function. If the probability of particle 1 created in a  $pp$  collision at rapidity  $y_1$  is independent of the probability of particle 2 having rapidity  $y_2$ , then the probability of particles 1 and 2 having rapidities  $y_1$  and  $y_2$  in the same event is

$$\frac{1}{n(\alpha\beta)} \rho_n^{\alpha\beta}(y_1^\alpha, y_2^\beta) = \frac{1}{n(\alpha)} \rho_n^\alpha(y_1^\alpha) \frac{1}{n(\beta)} \rho_n^\beta(y_2^\beta). \quad (5)$$

Thus we use the semi-inclusive correlation function  $\tilde{C}_n^{\alpha\beta}(y_1^\alpha, y_2^\beta)$  defined as

$$\tilde{C}_n^{\alpha\beta}(y_1^\alpha, y_2^\beta) \equiv \tilde{\rho}_n^{\alpha\beta}(y_1^\alpha, y_2^\beta) - \tilde{\rho}_n^\alpha(y_1^\alpha) \tilde{\rho}_n^\beta(y_2^\beta), \quad (6)$$

where

$$\tilde{\rho}_n^\alpha(y^\alpha) \equiv [1/n(\alpha)\sigma_n] d\sigma_n/dy^\alpha$$

and

$$\tilde{\rho}_n^{\alpha\beta}(y_1^\alpha, y_2^\beta) = [1/n(\alpha\beta)\sigma_n] d^2\sigma_n/dy_1^\alpha dy_2^\beta$$

are the one- and two-particle semi-inclusive probability densities. Relation (6) is illustrated in Fig. 20 using the (+ -) combination in 8-prong events as an example. It is seen that the values of  $\tilde{\rho}_8^{+-}(y_1^+, y_2^-)$  do not differ dramatically from the values of  $\tilde{\rho}_8^+(y_1^+) \tilde{\rho}_8^-(y_2^-)$ . The resulting values of the correlation function are therefore relatively small, e.g.  $\tilde{C}_8^{+-}(0, 0)/\tilde{\rho}_8^{+-}(0, 0) \approx 0.1$ . (We note that this ratio has similar values for all multiplicities and all charge combinations.) Nevertheless, definite trends are observed in the rapidity dependence of the  $\tilde{C}_n$  functions, as described in Sec. IV C.

## B. The inclusive and semi-inclusive correlations

To obtain a relation between the inclusive and semi-inclusive correlation functions we start from the additive property of the two-particle distribution,<sup>78, 79</sup>

$$\frac{d^2\sigma}{dy_1 dy_2} = \sum_n \frac{d^2\sigma_n}{dy_1 dy_2}, \quad (7)$$

and obtain

$$C^{\alpha\beta}(y_1^\alpha, y_2^\beta) = \langle n(\alpha\beta) \tilde{C}_n^{\alpha\beta}(y_1^\alpha, y_2^\beta) \rangle + X^{\alpha\beta}(y_1^\alpha, y_2^\beta), \quad (8)$$

TABLE IX. Results of fits to the semi-inclusive  $\pi^- x$  distributions of the form  $A \exp(-B|x|)$  over the interval  $0.02 < |x| < 0.04$ .

Multiplicity	A	
	(mb)	B
4	$0.39 \pm 0.02$	$2.5 \pm 0.6$
6	$1.03 \pm 0.09$	$5.1 \pm 0.5$
8	$1.33 \pm 0.23$	$6.0 \pm 1.7$
10	$1.64 \pm 0.13$	$7.6 \pm 0.9$
12	$1.83 \pm 0.22$	$10.5 \pm 1.0$
14	$1.04 \pm 0.09$	$10.9 \pm 1.0$
16	$0.63 \pm 0.13$	$13.2 \pm 4.0$

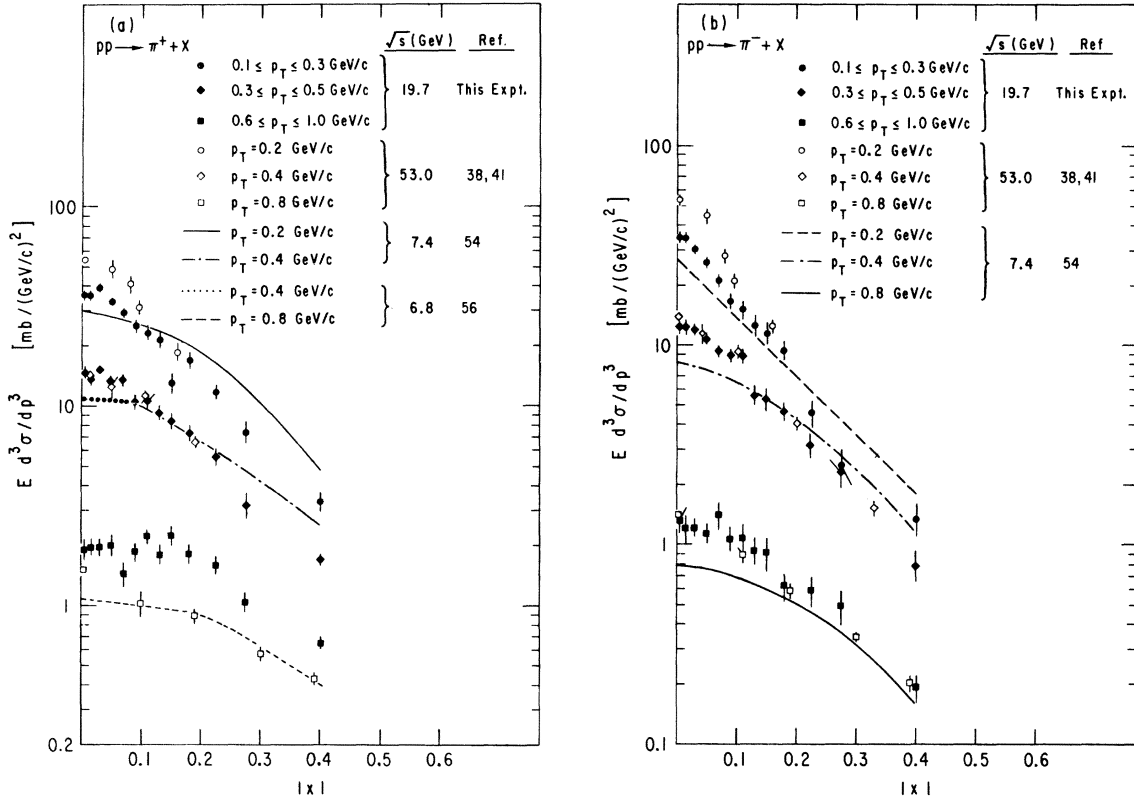


FIG. 17. The single-particle inclusive  $x$  distribution of (a) positive and (b) negative pions for three values of  $p_T$ .

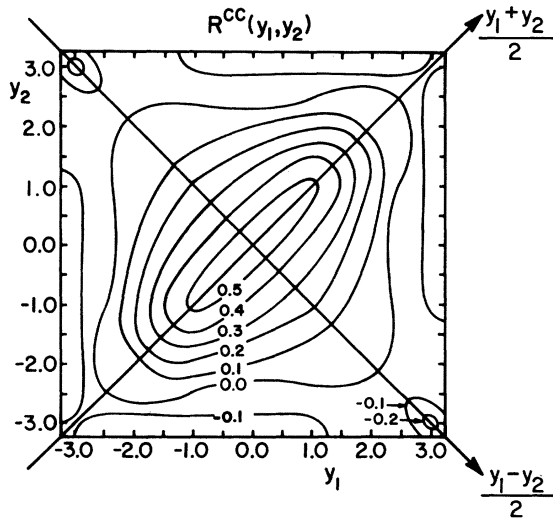


FIG. 18. Contours of  $R^{cc}(y_1, y_2) = \text{const}$  in the  $(y_1, y_2)$  plot. The curves were handdrawn through the data symmetrized about the  $y_1 = -y_2$  line. Typical error on the contours in the central region is  $\pm 0.03$ . (Bin sizes  $\Delta y_1 = \Delta y_2 = 0.5$ .) Positive particles with  $|x| > 0.6$  were excluded from the data shown in this figure.

where

$$\langle n(\alpha\beta) \bar{C}_n^{\alpha\beta}(y_1^\alpha, y_2^\beta) \rangle = \frac{\sum_n \sigma_n n(\alpha\beta) \bar{C}_n^{\alpha\beta}(y_1^\alpha, y_2^\beta)}{\sum_n \sigma_n} \quad (9)$$

and

$$\begin{aligned} X^{\alpha\beta}(y_1^\alpha, y_2^\beta) = & \sum_n \frac{\sigma_n}{\sigma} [\rho_n^\alpha(y_1^\alpha) - \rho^\alpha(y_1^\alpha)] \\ & \times [\rho_n^\beta(y_2^\beta) - \rho^\beta(y_2^\beta)] \\ & - \delta_{\alpha\beta} \sum_n n(\alpha) \rho_n^\alpha(y_1^\alpha) \rho_n^\beta(y_2^\beta). \end{aligned} \quad (10)$$

Thus, the inclusive correlation function can be written as a sum of two terms: the average semi-inclusive correlation function,  $\langle n(\alpha\beta) \bar{C}_n^{\alpha\beta}(y_1^\alpha, y_2^\beta) \rangle$ , and the term  $X^{\alpha\beta}(y_1^\alpha, y_2^\beta)$ , which depends on single-particle distributions only. Even if all the semi-inclusive correlation functions  $\bar{C}_n^{\alpha\beta}(y_1^\alpha, y_2^\beta)$  were zero, the inclusive correlation function would be nonzero, provided  $X^{\alpha\beta}(y_1^\alpha, y_2^\beta)$  is not zero. The first term in Eq. (10) will be equal to zero only when the single-particle distributions are the same for all multiplicities. Figure 6 shows that this is not the case. Also, for the like-particle combina-

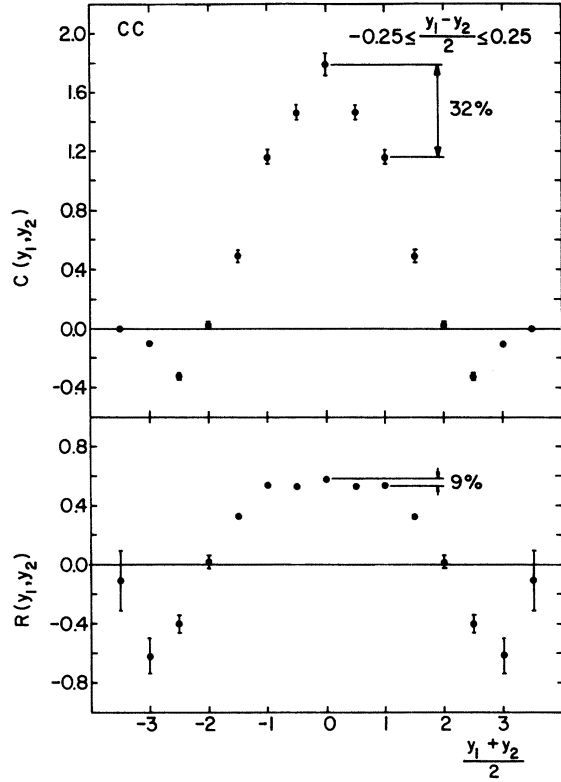


FIG. 19. The correlation functions  $C^{cc}(y_1, y_2)$  (upper part of the figure) and  $R^{cc}(y_1, y_2)$  (lower part) plotted against  $\frac{1}{2}(y_1 + y_2)$ , for a fixed value of  $\frac{1}{2}(y_1 - y_2) = 0$ .

tions, the first and second terms in Eq. (10) do not cancel each other in the data.

We therefore identify  $X^{\alpha\beta}(y_1^\alpha, y_2^\beta)$  as that part of the inclusive correlation function which results

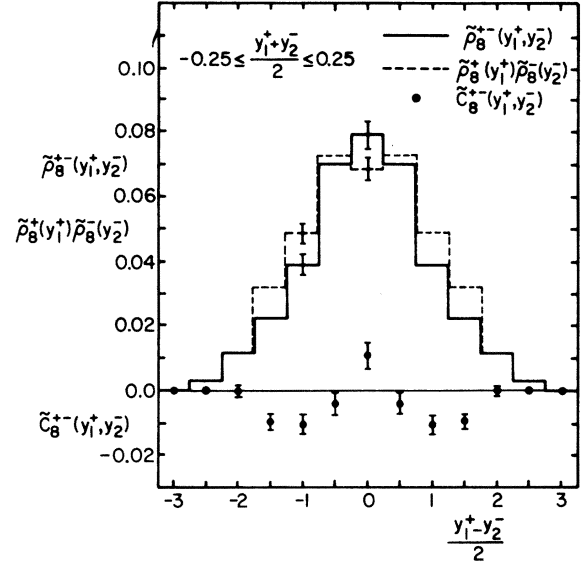


FIG. 20. Illustration of the definition of the semi-inclusive correlation function  $\tilde{C}_n^{\alpha\beta}(y_1^\alpha, y_2^\beta)$  for the  $+-$  combination in the 8-prong events. In addition, the product of the single-particle distributions (dashed line) and the two-particle distribution (solid line) are shown as a function of  $\frac{1}{2}(y_1^+ - y_2^-)$  for  $\frac{1}{2}(y_1^+ + y_2^-) = 0$ .

from including in the data events of different multiplicities ("mixing" the multiplicities). Figure 21 shows this effect for individual charge combinations. We notice the following features:

(i) The values of the inclusive correlation function  $C^{\alpha\beta}(y_1^\alpha, y_2^\beta)$  are positive for  $\frac{1}{2}|y_1^\alpha - y_2^\beta| \leq 2$ , for all charge combinations. The following inequalities hold for the central values:

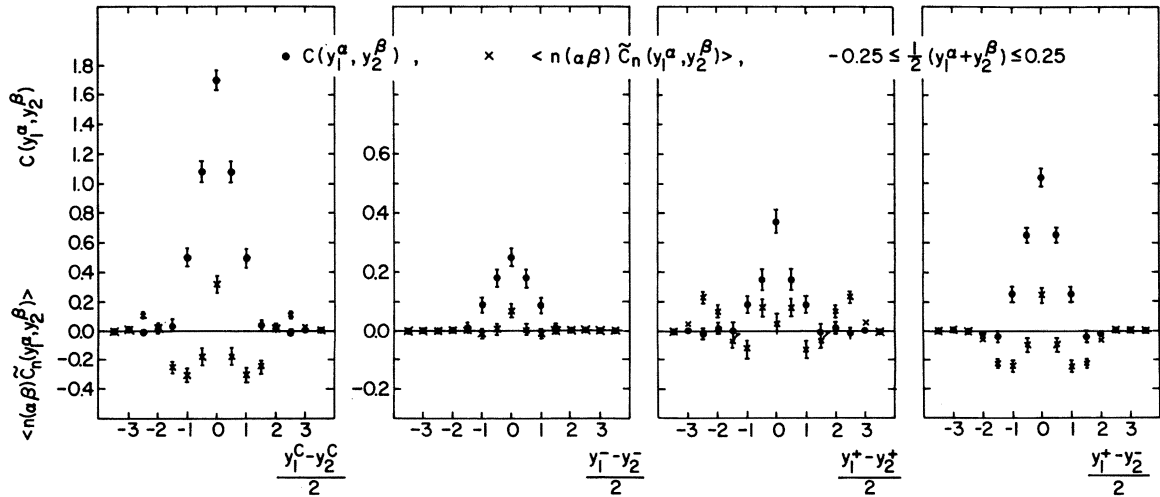


FIG. 21. The inclusive correlation function  $C(y_1^\alpha, y_2^\beta)$  (full circles), and the average semi-inclusive correlation function,  $\langle n(\alpha\beta) \tilde{C}_n^{\alpha\beta}(y_1^\alpha, y_2^\beta) \rangle$  (crosses) plotted against  $\frac{1}{2}(y_1^\alpha + y_2^\beta) = 0$ , for all four charge combinations. (No cuts were applied to the data in this figure.)

$$C^{cc}(0,0) > C^{+-}(0,0) > C^{++}(0,0) > C^{--}(0,0).$$

$C^{\alpha\beta}(y_1^\alpha, y_2^\beta)$  falls off relatively sharply from the peak values as  $|y_1^\alpha - y_2^\beta|$  increases.

(ii) If one interprets  $\langle n(\alpha\beta)\tilde{C}_n^{\alpha\beta}(y_1^\alpha, y_2^\beta) \rangle$  as the sum of a broad negative "background" and a central peak, one can notice that this peak is narrower than the inclusive  $C(y_1, y_2)$  and its height above the background is smaller than the magnitude of  $C(y_1, y_2)$ .

(iii) There is a noticeable structure in  $\langle n(\alpha\beta)\tilde{C}_n^{\alpha\beta}(y_1^\alpha, y_2^\beta) \rangle$  in the like-charge combinations, -- and ++, for small values of  $|y_1^\alpha - y_2^\beta|$ . For the ++ combination, the nonzero values of this function at large values of  $|y_1^+ - y_2^+|$  are due to the presence of leading protons (*all* particles were included in the data displayed in Fig. 21).

(iv) The large positive value of the inclusive correlation function in the central region is determined primarily by the multiplicity mixing term  $X^{\alpha\beta}(y_1^\alpha, y_2^\beta)$ .

Thus, in order to separate the influence of the multiplicity distribution on the correlation function from other dynamical effects, we turn to semi-inclusive distributions.

### C. The semi-inclusive correlations in rapidity

We have seen from the example of multiplicity mixing that the correlation functions can best serve as a tool for investigating processes in which only one production mechanism is involved, since a combination of production mechanisms with differing single-particle distributions gives rise to extraneous terms. This has been shown to be the case when diffractive and nondiffractive events are considered (see, e.g., Ref. 80). Since our aim is to study the production mechanism responsible for the bulk of multiparticle production, we concentrate our attention on nondiffractive events. We exclude charged multiplicities two and four which have a substantial fraction of diffractive events,<sup>7</sup> and focus our attention on the central region in the c.m. rapidity  $y$ . We also exclude leading particles by eliminating the identified slow protons ( $p_{\text{lab}} < 1.4$  GeV/c) and positive particles with  $x > 0.6$ , 97% of which are protons (see Sec. II D). However, had we proceeded in this way, we would have obtained events with  $n$ ,  $n-1$ , and  $n-2$  charged particles from a sample of events of charged multiplicity  $n$ . In order to keep a proper normalization of the semi-inclusive probability densities, we exclude two particles out of *every* event, namely the positive particles with the smallest and the largest c.m. rapidity  $y$  (or the slow and fast proton, if present). These cuts are applied to all data shown in the remainder of this section (as well as in Sec. V), and the reduced multiplicities are used to nor-

malize the probability densities. No attempt was made to correct the distributions for misassigning the pion mass to any unidentified heavier particles ( $K, p$ ) present in the data. However, a simulation by a Monte Carlo method indicated that the misidentification of heavier particles does not alter the main features of the correlation functions in the central region.

The values of  $\tilde{C}_n^{\alpha\beta}(y_1^\alpha, y_2^\beta)$  are displayed in Fig. 22 as a function of  $\frac{1}{2}(y_1^\alpha - y_2^\beta)$  for  $\frac{1}{2}(y_1^\alpha + y_2^\beta) = 0$  for multiplicities 6 through 14 and for the four possible charge combinations. It can be seen that:

the observed correlations are of short range, as  $\tilde{C}_n^{\alpha\beta}(y_1^\alpha, y_2^\beta)$  decreases sharply from its  $y_1 = y_2$  value;

the values in the central bin are  $\tilde{C}_n^{\alpha\beta}(0,0) \simeq 0.01$ , and are of comparable size for all charge combinations and all multiplicities;

the correlation function deviates systematically from zero for the +- and cc combinations, having the same characteristic shape for all multiplicities; and

for  $\frac{1}{2}(y_1^- - y_2^-) \neq 0$ , the values of  $\tilde{C}_n^{--}(y_1^-, y_2^-)$  deviate from zero less than the corresponding values for the other charge combination.

The region in  $\frac{1}{2}(y_1^+ - y_2^+)$ , where the values of  $\tilde{C}_n^{++}(y_1^+, y_2^+)$  are nonzero, is broader than in the -- case for most of the multiplicities. The difference between the ++ and -- combinations, which is represented mainly by the dip in  $\tilde{C}_n^{++}$  for  $\frac{1}{2}|y_1^+ - y_2^+| \simeq 1$ , seems to be less pronounced in ten- and higher-prong events than in events with lower multiplicity.

The  $(y_1 + y_2)$  dependence of the correlation functions is illustrated in Fig. 23 for the ten-prong events.<sup>81</sup> An approximate independence of  $\tilde{C}_n^{+-}(y_1^+, y_2^-)$  on  $(y_1^+ + y_2^-)$  can be noted for  $y_1^+ - y_2^- \simeq 0$  and for  $\frac{1}{2}|y_1^+ + y_2^-| \leq 1$ . The depth of the dip at  $\frac{1}{2}|y_1^+ - y_2^-| \simeq 1$  is, on the other hand, varying rapidly for increasing  $\frac{1}{2}|y_1^+ + y_2^-|$ . No such regularities are observed in the like-charge combinations. Similar trends are found in all multiplicities.

The features of the data presented in this subsection<sup>82</sup> contradict results of several experiments [100-GeV/c  $pp$  and  $\pi^+p$ ,<sup>83</sup> 147-GeV/c  $\pi^-p$  (Ref. 84)], where values of semi-inclusive correlation functions consistent with zero throughout the central region were reported for all charge combinations, and the absence of any short-range correlations was implied. On the other hand, our conclusions are, in general, supported by the results of other Fermilab experiments [100-GeV/c  $\pi^-p$ , 200-GeV/c  $pp$ , and 300-GeV/c  $pp$ ,<sup>85</sup> and 200-GeV/c  $\pi^-p$  (Ref. 86)], as well as by the results from ISR [Aachen-CERN-Heidelberg-Munich (ACHM) collaboration,<sup>87</sup> Pisa-Stony Brook (PS) collaboration<sup>88</sup>]. In Fig. 24 we replot our data for the cc combination following Ref. 87 (and Ref. 88), in order to compare our data

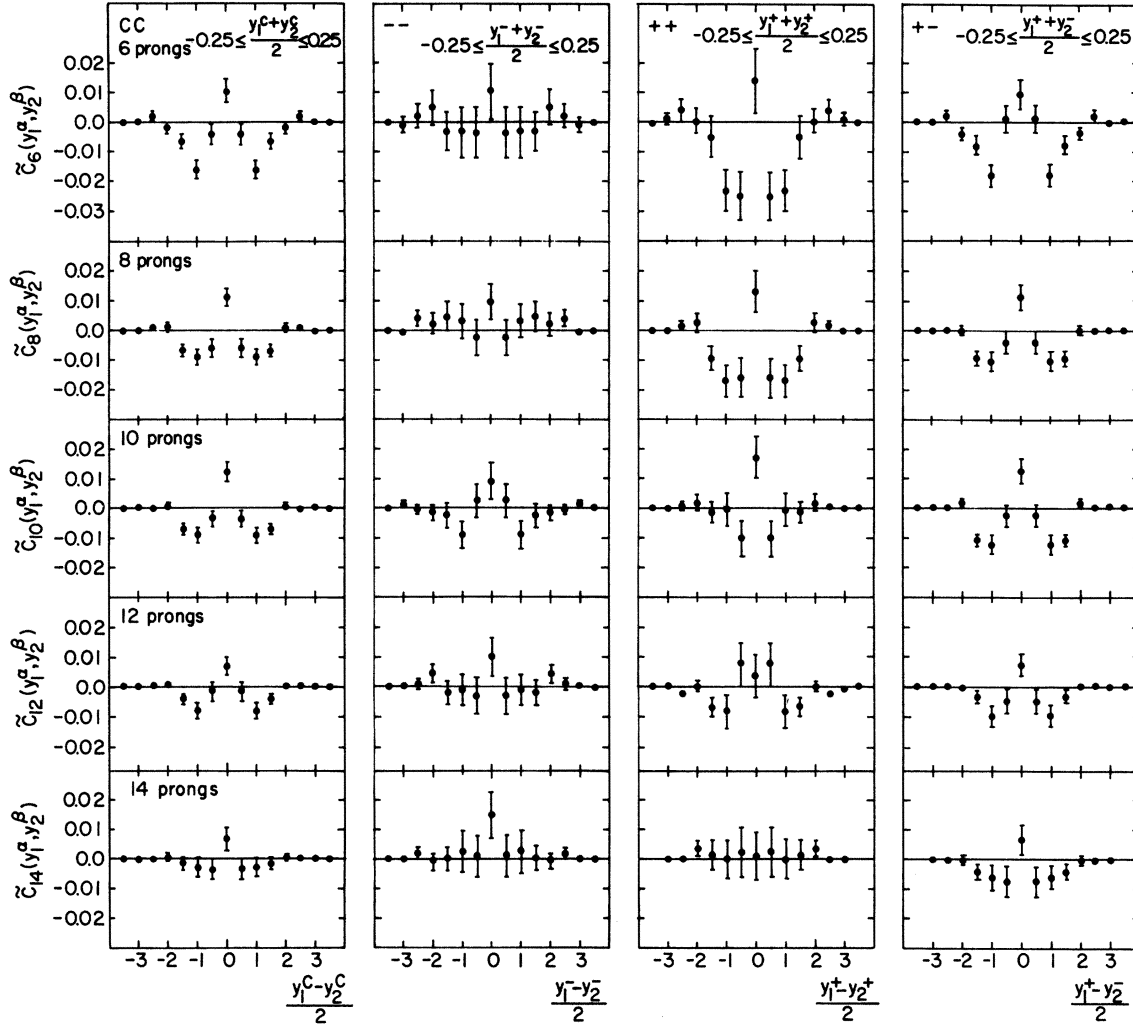


FIG. 22. The semi-inclusive correlation function  $\bar{C}_n^{\alpha\beta}(y_1^\alpha, y_2^\beta)$  plotted against  $\frac{1}{2}(y_1^\alpha - y_2^\beta)$  for a fixed value of  $\frac{1}{2}(y_1^\alpha + y_2^\beta) = 0$ , for multiplicities 6 through 14 and for all four charge combinations.

directly with the ISR results of the ACHM and PS collaborations for  $\sqrt{s} = 23$  GeV. Here the c.m. pseudorapidity  $\eta$  is used as the independent variable, and all particles with  $|\eta| > 2.25$  are excluded. The redefined charged multiplicity  $n$  is limited to the interval between 6 and 15. No other cuts are applied to our data, i.e., the identified protons are included as such. It is seen that the central values of the average semi-inclusive correlation function for all three experiments are compatible with each other. The disagreement for  $\frac{1}{2}|\eta_1 - \eta_2| \gtrsim 2$  can be attributed to the opposite directions in which rapidities of the misidentified heavy particles are shifted in the two experimental arrangements (see Sec. II D).

The semi-inclusive correlation function can be parametrized by the form

$$\bar{C}_n^{\alpha\beta}(y_1^\alpha, y_2^\beta) = a_n \left\{ \frac{\bar{\rho}_n^c(0)}{2\delta_n \sqrt{\pi}} \exp[-(y_1^\alpha - y_2^\beta)^2 / 4\delta_n^2] - \bar{\rho}_n^\alpha(y_1^\alpha) \bar{\rho}_n^\beta(y_2^\beta) \right\} \quad (11)$$

obtained by modifying the results of Ref. 89 (based on the independent-cluster-emission model) for the definition of the correlation function used in this report. An example of this parametrization is given in Fig. 25 showing the data on  $\bar{C}_{10}^c(y_1^c, y_2^c)$  together with a curve representing a fit of the form of Eq. (11) to the data (solid line). The two terms on the right-hand side of Eq. (11) are also shown separately: the Gaussian term, after subtracting  $a_{10}[\bar{\rho}_{10}^c(0)]^2$  (dashed line), and the "background term" (dashed-dotted line). It is seen that the solid line represents the data reasonably well.

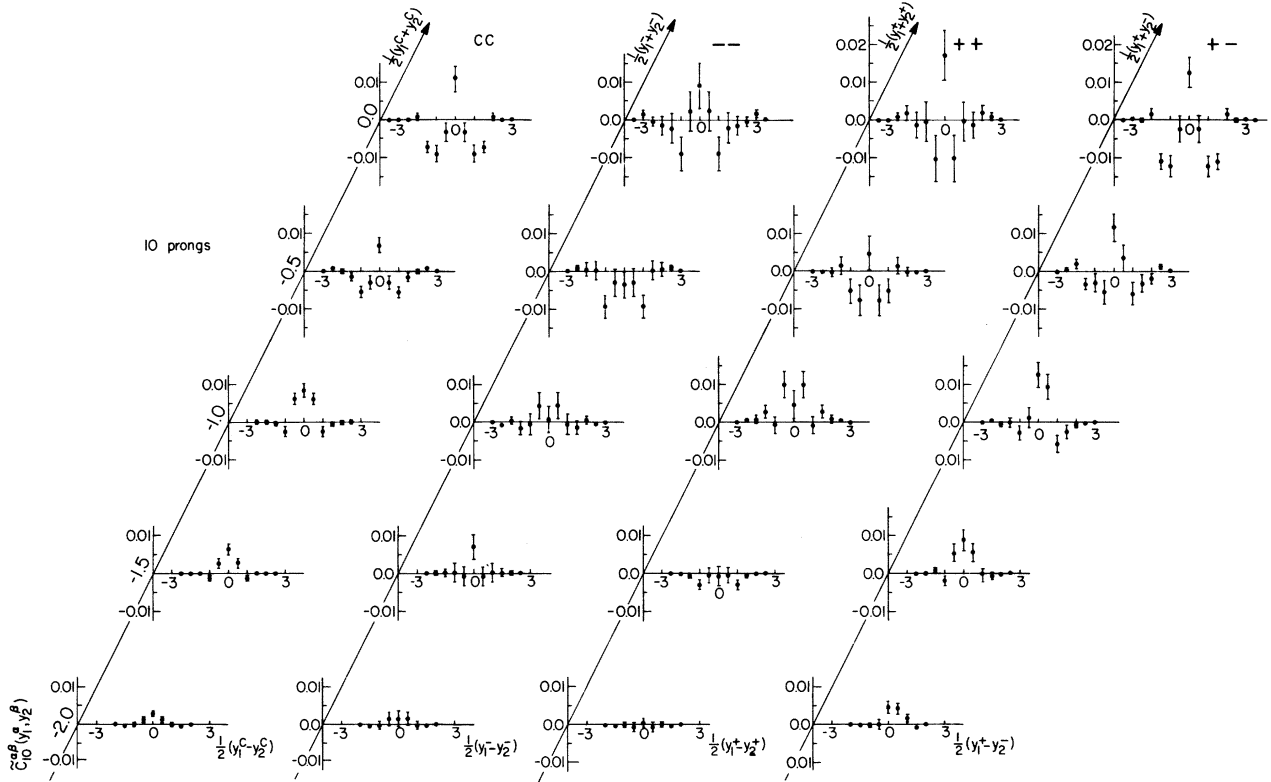


FIG. 23. The semi-inclusive correlation function  $\tilde{C}_{10}^{cc}(\eta_1^{\alpha}, \eta_2^{\beta})$  for 10-prong events and all charge combinations plotted against  $\frac{1}{2}(\eta_1^{\alpha} - \eta_2^{\beta})$  for all values of  $\frac{1}{2}(\eta_1^{\alpha} + \eta_2^{\beta})$ .

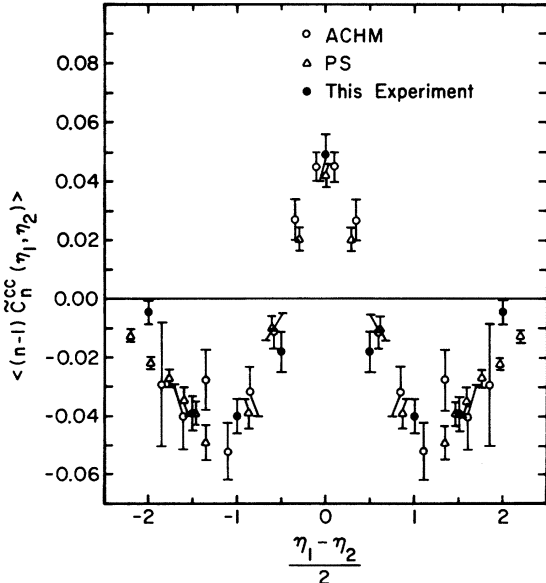


FIG. 24. The average semi-inclusive correlation function in the center-of-mass pseudorapidity  $\eta$ ,  $\langle (n-1) \tilde{C}_n^{cc}(\eta_1, \eta_2) \rangle$ , for the  $cc$  combination. Only particles with  $|\eta| \leq 2$  are included. The results of ISR experiments at  $\sqrt{s} = 23$  GeV (ACHM, Ref. 87—open circles, and PS, Ref. 88—triangles) are averaged over  $\eta_1 + \eta_2$ , while data of this experiment ( $\sqrt{s} = 19.7$  GeV, full circles) are for  $-0.25 \leq \frac{1}{2}(\eta_1 + \eta_2) \leq 0.25$ .

The  $(\eta_1 - \eta_2)$  dependence of the correlation function was fitted to the expression (11) for  $\frac{1}{2}(\eta_1 + \eta_2) = 0$  using the measured values for the single-particle densities. The values of the parameters  $a_n$  and  $\delta_n$  are shown in Fig. 26 as a function of charged multiplicity,  $n_{ch}$ , for the  $cc$  and  $+ -$  combinations. The values of the width of the Gaussian term,  $\delta_n$ , are consistent with being multiplicity independent. The values of  $\delta_n$  in the  $+ -$  case are somewhat lower than in the  $cc$  case, but the two are compatible with having a common value between 0.5 and 0.6. The values of the parameter  $a_n$  decrease with the multiplicity for all charge combinations.

We note that our results for  $\delta_n^{cc}$  are compatible with the values reported both by the PS collaboration,  $\delta_n^{cc} = 0.62 \pm 0.05$ ,<sup>88</sup> and by the ACHM collaboration,  $\delta_n^{cc} = 0.65 \pm 0.08$  (Ref. 87) (obtained from the correlation function averaged over multiplicity).

For a possible physical interpretation of Eq. (11) we turn to the independent-cluster-emission model.<sup>89</sup> In this model, only particles resulting from a decay of the same cluster contribute to correlations, as characterized by the first term on the right-hand side of Eq. (11). The parameter  $\delta_n$  characterizes the single-particle distribution of the cluster decay products in the cluster rest

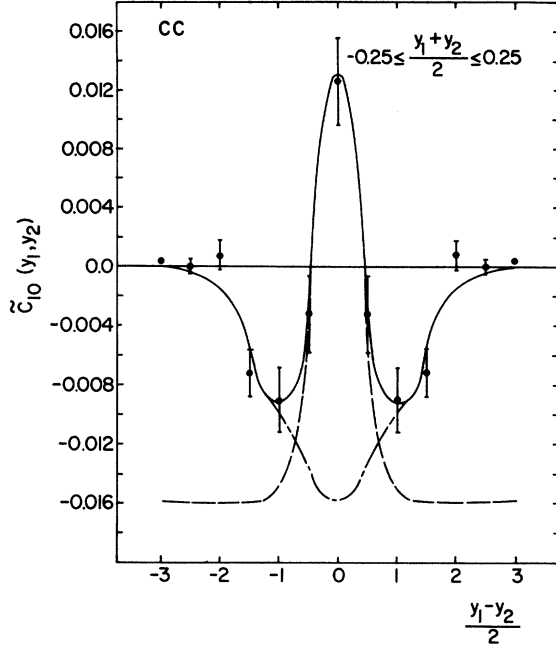


FIG. 25. The semi-inclusive correlation function  $\tilde{C}_{10}(y_1, y_2)$  for the  $cc$  combination in ten-prong events plotted against  $\frac{1}{2}(y_1 - y_2)$  for a fixed value of  $\frac{1}{2}(y_1 + y_2) = 0$ . The lines represent a parametrization of the data according to Eq. (11): The dashed line represents the first term in Eq. (11) after subtracting  $a_{10}[\beta_{10}^c(0)]^2$ , the dashed-dotted line represents the second term, and the solid line is the sum of the two terms. (The solid line is drawn whenever the dashed line or the dashed-dotted line and the solid line coincide.)

frame. The first two moments of the multiplicity distribution of the cluster decay are contained in  $a_n$ :

$$a_n = \frac{n}{n(\alpha\beta)} \left( \frac{\langle k(\alpha\beta) \rangle}{\langle k \rangle} \right)_n,$$

where  $\langle k \rangle_n$  is the average cluster-decay charged multiplicity in an  $n$ -hadron final state, and  $\langle k(\alpha\beta) \rangle_n$  is the average number of two-particle combinations in an  $n$ -hadron final state in which one particle is of type  $\alpha$  and the other is type  $\beta$ , both from the decay of the same cluster. The  $n$  dependence of the quantity  $A_n = \langle \langle k(\alpha\beta) \rangle / \langle k \rangle \rangle_n$  is related to the cluster-decay multiplicity distribution<sup>89,88</sup>:  $A_n$  does not depend on  $n$  in the case when all clusters decay into a fixed number of particles, and it increases with  $n$  if the cluster-decay multiplicity distribution is broader.

The  $n$  independence of the width  $\delta_n$  lends support to the idea that the clusters are entities with multiplicity-independent characteristics: The distributions of the cluster decay products do not depend on the overall multiplicity. The values of  $A_n$ , calculated using the values of  $a_n$  from Fig. 26, are

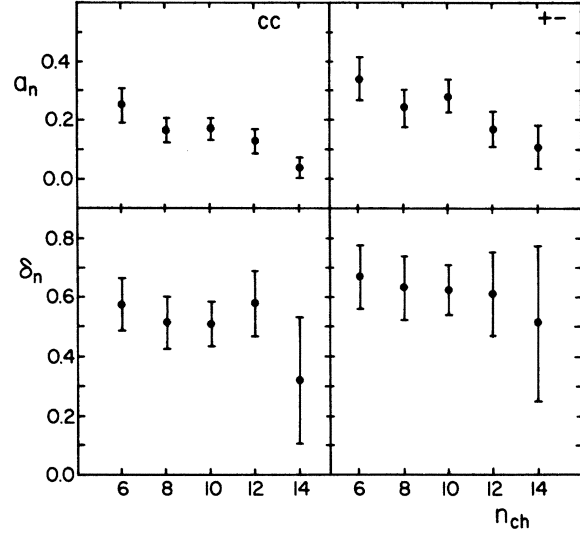


FIG. 26. Parameters of the fit of the form of Eq. (11) to the semi-inclusive correlation function  $\tilde{C}_n^{\alpha\beta}(y_1^\alpha, y_2^\beta)$  for the  $cc$  and  $+ -$  charge combinations as a function of the charged multiplicity  $n_{ch}$ .

given in Table X. The data indicate an increase of  $A_n$  with increasing  $n$ , thus suggesting that the clusters do not decay into a fixed number of particles. It is not possible to obtain from the data more specific information about the cluster-decay multiplicity distribution (e.g. its moments) without making assumptions about its form. Let us add that our results for  $A_n$  in the case of the  $cc$  combination agree with the more precise ISR data of Ref. 88.

Equation (11) would describe the data in a larger  $(y_1, y_2)$  interval, if an exact translational invariance were a property of  $\tilde{C}_n(y_1, y_2)$ . Since this is not the case in our data, as observed in Fig. 23, it is not surprising to find that no satisfactory fit of the form of Eq. (11) was obtained using all data for  $|y_1| \leq 2$ ,  $|y_2| \leq 2$ .

#### D. Joint correlations in rapidity and the azimuthal angle

Further information on two-particle distributions can be obtained by investigating the distributions in the plane transverse to the beam direction. There are three independent variables de-

TABLE X. Parameters of the cluster-decay multiplicity distribution.

$n_{ch}$	$\left[ \frac{\langle k(cc) \rangle}{\langle k(c) \rangle} \right]_n$	$\left[ \frac{\langle k(+ -) \rangle}{\langle k(c) \rangle} \right]_n$
6	$0.75 \pm 0.17$	$0.33 \pm 0.08$
8	$0.83 \pm 0.21$	$0.37 \pm 0.09$
10	$1.21 \pm 0.25$	$0.56 \pm 0.11$
12	$1.18 \pm 0.36$	$0.43 \pm 0.15$

scribing the transverse momenta of a pair of particles:  $p_{T1}$ ,  $p_{T2}$ , and  $\phi_1 - \phi_2$ . [Here  $\phi_i$  ( $i=1,2$ ) is the angle between  $\vec{p}_{Ti}$  and an arbitrary fixed direction in the transverse plane.]

Owing to the limited size of our data sample,

we cannot study two-particle cross sections as a function of all five variables ( $y_1, y_2, p_{T1}, p_{T2}, \phi \equiv \phi_1 - \phi_2$ ). We therefore integrate the semi-inclusive correlation function  $\bar{C}_n^{\alpha\beta}(\vec{p}_1^\alpha, \vec{p}_2^\beta)$  over the magnitudes of the transverse momenta and obtain

$$\bar{C}_n^{\alpha\beta}(y_1^\alpha, y_2^\beta, \phi^{\alpha\beta}) = \frac{1}{n(\alpha\beta)\sigma_n} \frac{d\sigma_n}{dy_1^\alpha dy_2^\beta d\phi^{\alpha\beta}} - \int \frac{1}{n(\alpha)\sigma_n} \frac{d\sigma_n}{dy_1^\alpha d\phi_1^\alpha} \frac{1}{n(\beta)\sigma_n} \frac{d\sigma_n}{dy_2^\beta d\phi_2^\beta} d\phi_1^\alpha d\phi_2^\beta \delta(\phi_1^\alpha - \phi_2^\beta - \phi^{\alpha\beta}). \quad (12)$$

Since it is impractical to present the data for all multiplicities, we present results on  $\bar{C}_n^{\alpha\beta}(y_1^\alpha, y_2^\beta, \phi^{\alpha\beta})$  for the ten-prong events as a typical semi-inclusive sample. The function  $\bar{C}_{10}^{\alpha\beta}$  is plotted in Fig. 27 against  $\frac{1}{2}(y_1^\alpha - y_2^\beta)$  and  $\phi^{\alpha\beta}$  for a fixed value of  $\frac{1}{2}(y_1^\alpha + y_2^\beta) = 0$ . All four charge combinations are shown. We note the following salient features:

(a) For the unlike-charge combination,  $+ -$ , the correlation function attains its largest value for  $y_1^+ = y_2^- = 0$  and  $135^\circ < \phi^{+-} < 180^\circ$ ; the rate of decrease of the correlation function from its central value is also largest in this  $\phi^{+-}$  interval;

(b) For the like-charge combinations,  $--$  and  $++$ , the largest value and the steepest slope are found for  $0^\circ < \phi^{\alpha\alpha} < 45^\circ$ ;

(c)  $\bar{C}_{10}^{cc}$  has relatively large peaks for both small and large  $\phi$ .

These features agree qualitatively with previously reported ISR data ( $cc$  combination),<sup>87</sup> as well as with results from Fermilab.<sup>20, 85, 86</sup>

A more detailed view of the data is offered by Fig. 28 which shows  $\bar{C}_{10}^{\alpha\beta}(y_1^\alpha, y_2^\beta, \phi^{\alpha\beta})$  plotted as a function of  $\frac{1}{2}(y_1^\alpha - y_2^\beta)$  and  $\phi^{\alpha\beta}$  for four intervals in  $\frac{1}{2}(y_1^\alpha + y_2^\beta)$ . The data for the  $+ -$  combination [Fig. 28(a)] show that the tendency of the  $y_1^+ = y_2^-$  values of the correlation function to be larger for  $\phi^{+-} > 90^\circ$  than for  $\phi^{+-} < 90^\circ$  persists for nonzero values of  $\frac{1}{2}(y_1^+ + y_2^-)$ . The data for  $\bar{C}_{10}^{--}(y_1^-, y_2^-, \phi^{--})$  [Fig. 28(b)] indicate that  $\phi < 90^\circ$  is preferred in the like-particle combinations. A significant peak is observed at  $y_1^- = y_2^-$  and  $\phi^{--} < 45^\circ$  for  $y_1^- + y_2^- = 0$ .

We have seen above that several features of the rapidity correlation functions can be understood in terms of the independent-cluster-emission model. Use of such a model raises the question of the nature of the clusters. It has been suggested<sup>90</sup> that the clusters are actually resonances familiar from particle scattering in the few-GeV region. The observed two-particle correlations would then be naturally explained as reflections of the relation-

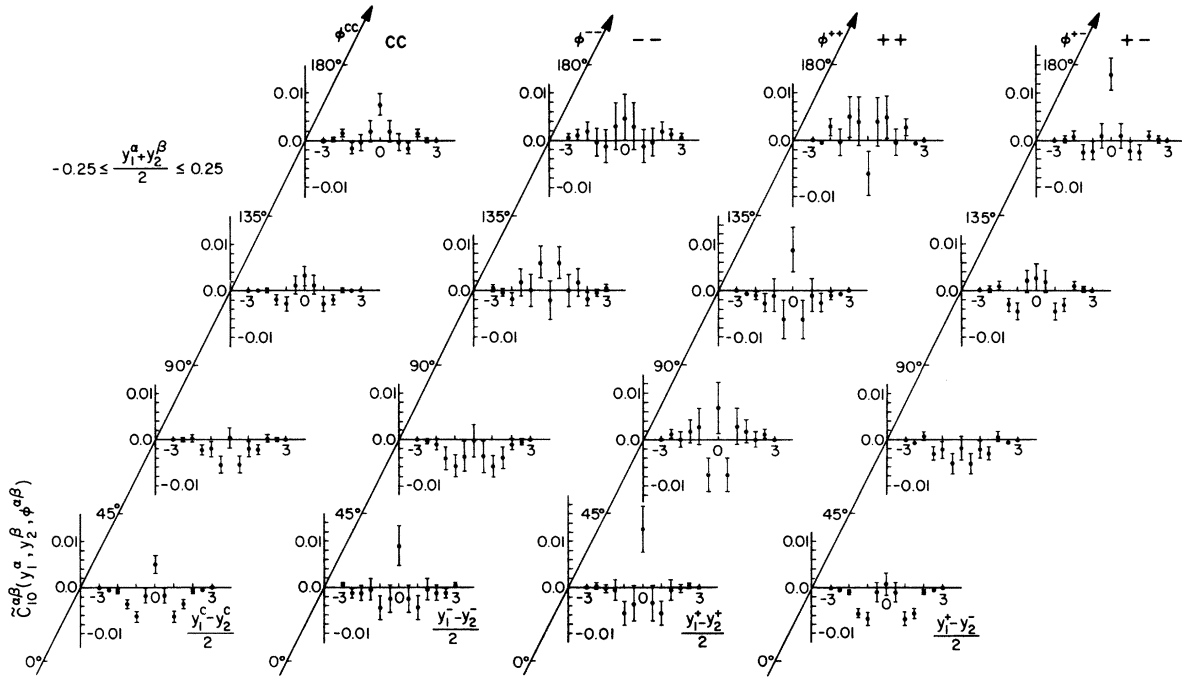


FIG. 27. The semi-inclusive correlation function  $\bar{C}_{10}^{\alpha\beta}(y_1^\alpha, y_2^\beta, \phi^{\alpha\beta})$  plotted against  $\frac{1}{2}(y_1^\alpha - y_2^\beta)$  for a fixed value of  $\frac{1}{2}(y_1^\alpha + y_2^\beta) = 0$ , in four bins in the azimuthal angle  $\phi^{\alpha\beta}$ , for all charged combinations.

ship between decay products of a resonance. Indeed, the production of the  $\rho^0$  resonance has been observed in our data<sup>26</sup> with most of the cross section coming from the central region. Moreover, it has been observed<sup>26</sup> that  $\rho^0$  production is en-

hanced if the decay products, a  $\pi^+$  and a  $\pi^-$ , move "back-to-back" in the transverse plane ( $\phi > 90^\circ$ ). This would naturally explain the origin of the peak in  $\bar{C}_{10}^{\alpha\beta}(y_1^+, y_2^-, \phi^{\alpha\beta})$  for  $y_1^+ = y_2^-$  in the  $\phi^{\alpha\beta} > 135^\circ$  bin. This view is also supported by the results of a

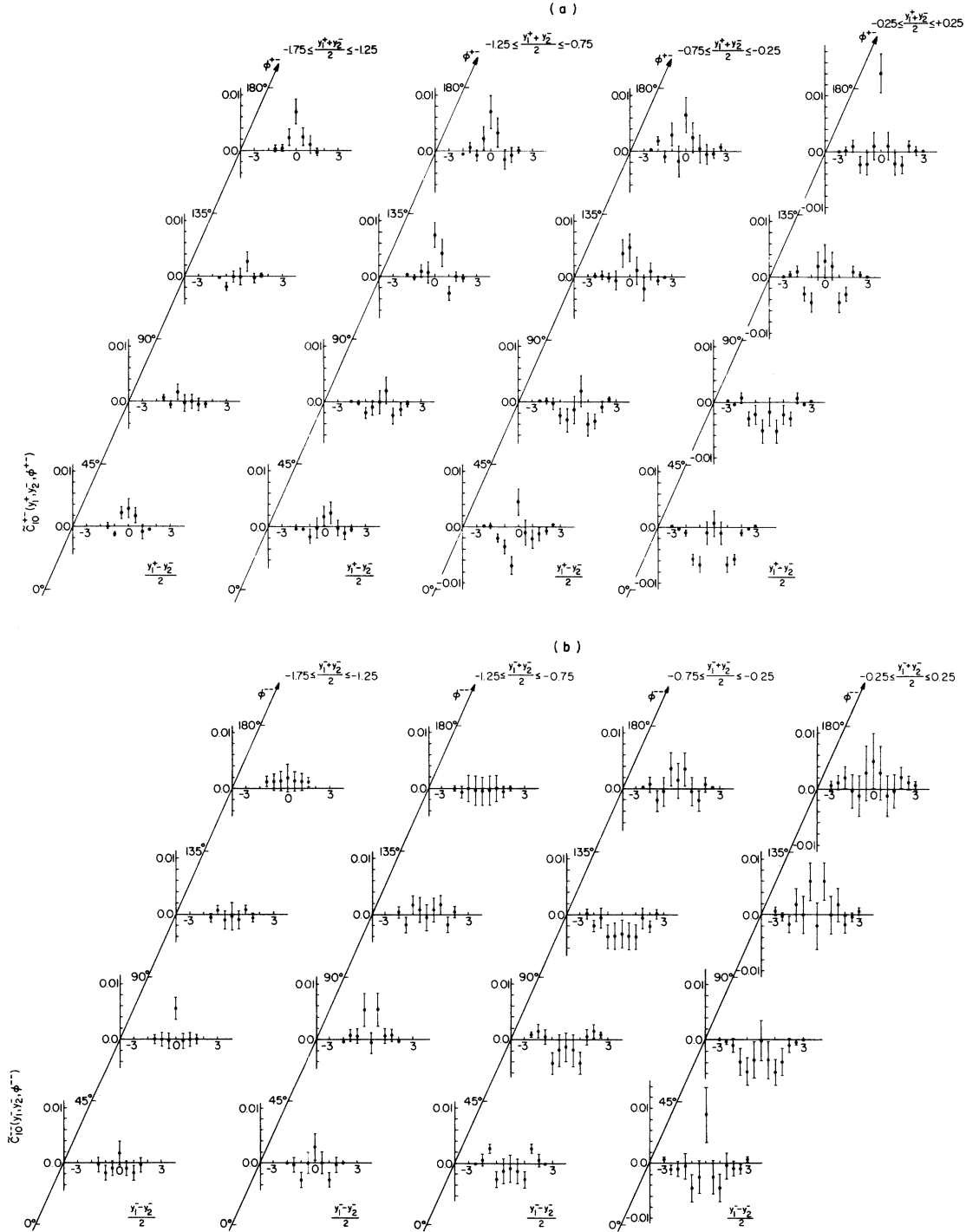


FIG. 28. The semi-inclusive correlation function  $\bar{C}_{10}^{\alpha\beta}(y_1^{\alpha}, y_2^{\beta}, \phi^{\alpha\beta})$  plotted against  $\frac{1}{2}(y_1^{\alpha} - y_2^{\beta})$  for all values of  $\frac{1}{2}(y_1^{\alpha} + y_2^{\beta})$  in four bins in the azimuthal angle  $\phi^{\alpha\beta}$ : (a) for the  $+-$  and (b)  $--$  charge combinations.

Monte Carlo calculation based on a model incorporating the production of  $\rho$ ,  $\omega$ , and  $\eta$ .<sup>87</sup> In this model, the peak in the correlation  $\bar{C}_n^{cc}(y_1^c, y_2^c, \phi^{cc})$  for  $\phi^{cc} > 135^\circ$  appears to be a consequence of  $\rho^0$  production and its subsequent decay. The peak for  $\phi^{cc} < 45^\circ$  can, under certain conditions, be explained in this model as a correlation between the decay products of  $\omega$  or  $\eta$  (decaying into a  $\pi^+$ , a  $\pi^-$ , and a  $\pi^0$ ).<sup>91</sup> This hypothesis is not contradicted by our data, where a definite correlation in the  $+ -$  combination is observed for  $\phi^{+-} < 45^\circ$  [Fig. 28(a)].

However, a substantial contribution to  $\bar{C}_n^{cc}(y_1^c, y_2^c, \phi^{cc})$  for  $\phi^{cc} < 45^\circ$  comes from the like-charge combinations (Fig. 27). The character of the latter, namely the fact that the enhancement is confined to  $\phi^{--} < 90^\circ$  [see Fig. 28(b)], is strongly suggestive of the fact that it is of quite a different physical origin than the structure of correlations in the case of the  $+ -$  combination. The conjecture has been made that the observed peak in the correlation functions for the like-charge combinations is an effect of Bose-Einstein statistics of the pions.<sup>20</sup> (Such effects were hypothesized a long time ago for  $\bar{p}p$  collisions.<sup>92</sup>)

#### E. Two-particle correlations in transverse momentum

We complete our discussion of two-particle distributions with a study of a variable heretofore integrated over, namely the magnitude of the transverse momentum. Recent measurements of  $p_T$  distributions have yielded results rich in interesting dynamical features in the region of large  $p_T$ .<sup>93</sup> For a better understanding of the large- $p_T$  phenomena it is helpful to know the behavior of the low- $p_T$  "background," i.e., a region in  $p_T$  which is accessible in a bubble-chamber experiment.

We first look at the inclusive and semi-inclusive two-particle distributions integrated over the longitudinal momenta, as well as over the azimuthal angle,  $\rho(p_{T1}, p_{T2}) \equiv (1/\sigma) d\sigma/dp_{T1} dp_{T2}$  and  $\rho_n(p_{T1}, p_{T2}) \equiv (1/\sigma_n) d\sigma_n/dp_{T1}, dp_{T2}$ . These can be compared with a suitable combination of single-particle  $p_T$  distributions using the correlation-function formalism used previously for the rapidity distributions. Repeating the steps of Secs. IV B and IV C we observe relative large values of a smoothly varying inclusive correlation function. Its main component is the "multiplicity mixing term" containing only single-particle distributions. No systematic trends reflecting dynamic features are observed in our data on the semi-inclusive correlation function,

$$\bar{C}_n(p_{T1}, p_{T2}) \equiv \bar{\rho}_n(p_{T1}, p_{T2}) - \bar{\rho}_n(p_{T1}) \bar{\rho}_n(p_{T2}).$$

We therefore present our results for two inte-

grated measures of correlations: the average associated charged multiplicity<sup>94</sup>

$$\langle n_1^\alpha(\vec{p}_2^\beta) \rangle = \frac{\int \frac{d\sigma}{d\vec{p}_1^\alpha d\vec{p}_2^\beta} d\vec{p}_1^\alpha}{\frac{d\sigma}{d\vec{p}_2^\beta}} \quad (13)$$

and the average associated transverse momentum<sup>95</sup>

$$\langle p_{T1}^\alpha(p_{T2}^\beta) \rangle = \frac{\int \frac{d\sigma}{d\vec{p}_1^\alpha d\vec{p}_2^\beta} p_{T1}^\alpha d\vec{p}_1^\alpha}{\int \frac{d\sigma}{d\vec{p}_1^\alpha d\vec{p}_2^\beta} d\vec{p}_1^\alpha}. \quad (14)$$

The integration region extends over all values of  $p_{T1}$  and over suitable regions in the rapidities  $y_1$  and  $y_2$  and the azimuthal angle  $\phi$ , as specified below. (As before,  $\alpha$  and  $\beta$  label the particles' charge state.)

Figure 29 (Ref. 96) shows the average associated multiplicity  $\langle n_1^\alpha(p_{T2}^\beta; \phi^{\alpha\beta}) \rangle$  for all charge combina-

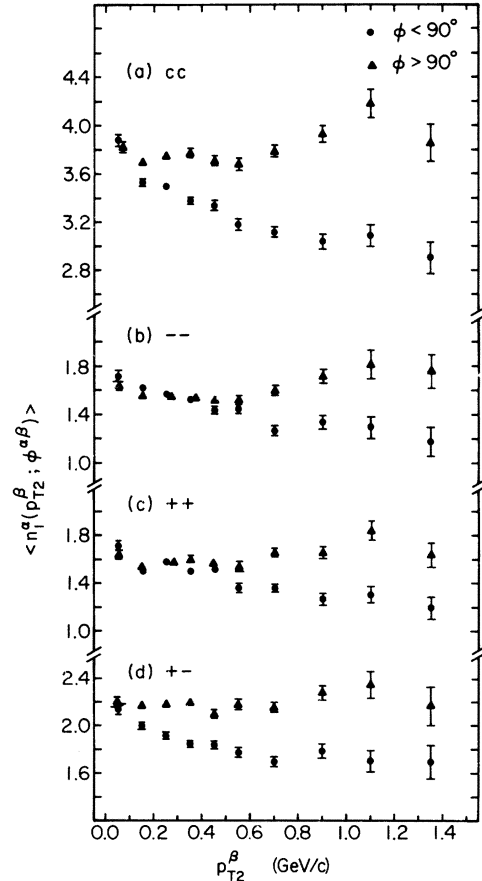


FIG. 29. The average associated multiplicity,  $\langle n_1^\alpha(p_{T2}^\beta; \phi^{\alpha\beta}) \rangle$  in two  $\phi^{\alpha\beta}$  intervals, for all charge combinations. (The particle at  $p_T$  is not counted in the associated multiplicity.)

tions, obtained from Eq. (13) by integrating over the full range of  $y_1$  and  $y_2$ , and over two  $\phi^{\alpha\beta}$  intervals:  $0^\circ < \phi^{\alpha\beta} < 90^\circ$  ("same-side particles"; full circles), and  $90^\circ < \phi^{\alpha\beta} < 180^\circ$  ("opposite-side particles"; triangles). The general trend of the data for  $\langle n_1^\alpha(p_{T2}^\beta) \rangle$  (obtained by adding together both  $\phi^{\alpha\beta}$  intervals) is to decrease with increasing  $p_{T2}^\beta$ . This is consistent with the previously observed multiplicity dependence of semi-inclusive  $\langle p_T \rangle_n$  (Sec. III B): Finding a particle at larger  $p_T$  means an increased probability of having an event of lower multiplicity. When comparing the trends of data in the two  $\phi$  intervals, it is the associated multiplicity of the same-side particles which is decreasing with increasing  $p_{T2}$ , while the multiplicity of the opposite-side particles tends to be independent of  $p_{T2}$ .

A noticeable difference is observed between the behavior of the like- and unlike-particle combinations. In the -- and ++ charge combinations there is little difference between the multiplicity of same-side and opposite-side particles for  $p_{T2}^\beta \leq 0.5$  GeV/c, with the same-side multiplicity being

the larger of the two for the lowest  $p_{T2}$  bins. On the other hand, the opposite-side multiplicity is significantly larger than the same-side multiplicity for all  $p_{T2} \geq 0.1$  GeV/c in the +- combination. For  $p_{T2}^\beta \geq 0.6$  GeV/c, the multiplicity for  $\phi^{\alpha\beta} > 90^\circ$  is larger than that for  $\phi^{\alpha\beta} < 90^\circ$  for all charge combinations. A similar trend is observed in semi-inclusive data (not shown), with the difference between the like- and unlike-particle combinations at small  $p_{T2}$  being more pronounced at higher multiplicities.

The difference between the like- and unlike-charge combinations is illustrated in greater detail in Fig. 30, where the dependence of the average associated multiplicity on the rapidity separation is displayed.  $\langle n_1^\alpha(p_{T2}^\beta; \Delta y^{\alpha\beta}, \phi^{\alpha\beta}) \rangle$  is obtained from Eq. (13) by keeping  $\Delta y^{\alpha\beta} \equiv |y_1^\alpha - y_2^\beta|$  within a given interval and integrating over all  $(y_1^\alpha + y_2^\beta)$ . The difference between the -- and +- combinations observed before (Fig. 29) is most pronounced for small  $\Delta y^{\alpha\beta}$ . The multiplicity for  $\phi^{\alpha\beta} < 90^\circ$  is larger than the multiplicity for  $\phi^{\alpha\beta} > 90^\circ$  for small

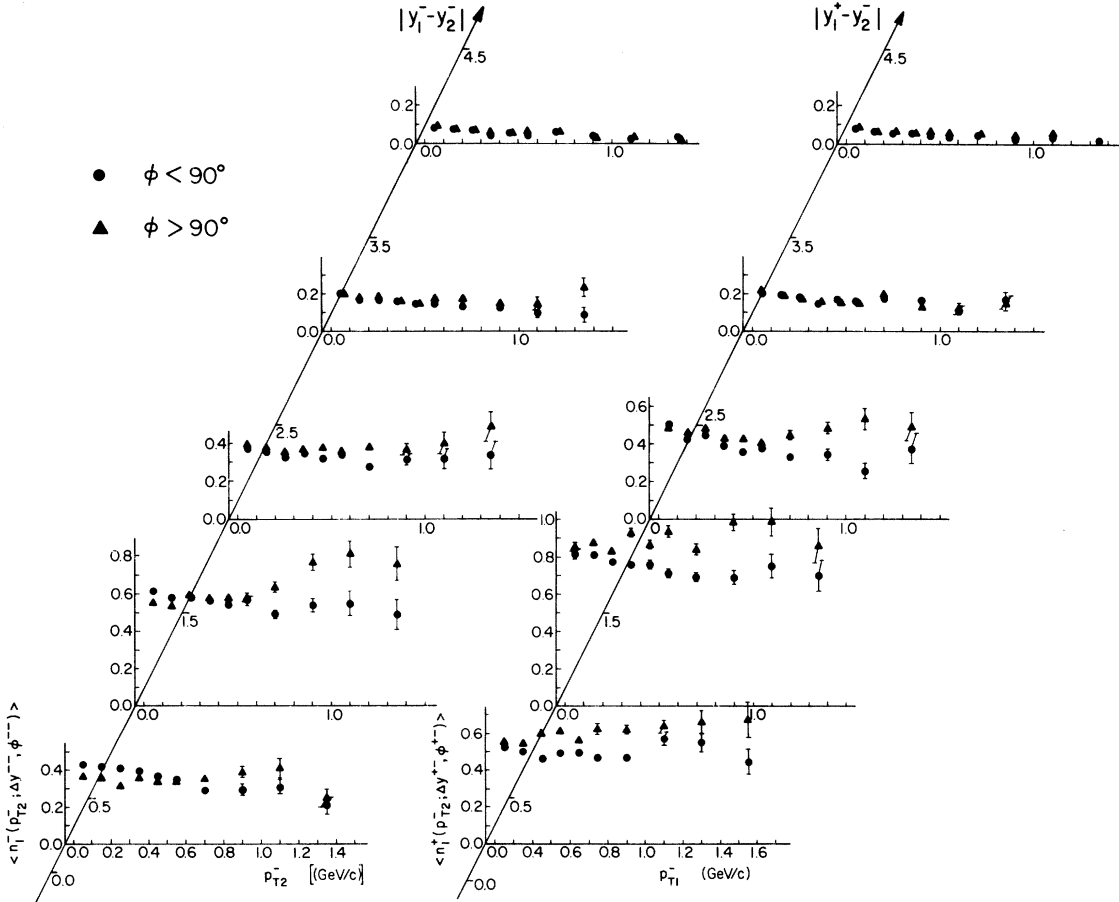


FIG. 30. The average associated multiplicity,  $\langle n_1^\alpha(p_{T2}^\beta; \Delta y^{\alpha\beta}, \phi^{\alpha\beta}) \rangle$  in two  $\phi^{\alpha\beta}$  intervals and five bins in the rapidity separation,  $\Delta y^{\alpha\beta}$ , for the -- and +- charge combinations.

$p_{T2}^\beta$  in the -- case, while the opposite holds true for the +- case. To a smaller degree this effect is also observed in the interval  $0.5 < \Delta y^{\alpha\beta} < 1.5$ . For larger  $\Delta y^{\alpha\beta}$ , the opposite-side multiplicity is the larger one for all  $p_{T2}^\beta$  and all charge combinations, with the difference between the same-side and opposite-side multiplicities disappearing at the largest rapidity separations.

The fact that the multiplicity of like particles in the same transverse momentum direction is enhanced at small rapidity separations and small  $p_T$  suggests the interpretation of this effect as a consequence of the Bose-Einstein statistics of like particles. Similar trends were also observed in  $pp$  data at 69 GeV/c.<sup>97</sup>

The other quantity considered in this section, the average associated transverse momentum, is displayed in Fig. 31 in two  $\phi^{\alpha\beta}$  bins, integrated over all  $y_1^\alpha$  and  $y_2^\beta$  values. The overall tendency of  $\langle p_{T1}^\alpha(p_{T2}^\beta) \rangle$  is to increase with increasing  $p_{T2}^\beta$ . In view of the  $p_{T2}^\beta$  dependence of the associated multiplicity described above, such a qualitative behavior is required by momentum conservation.

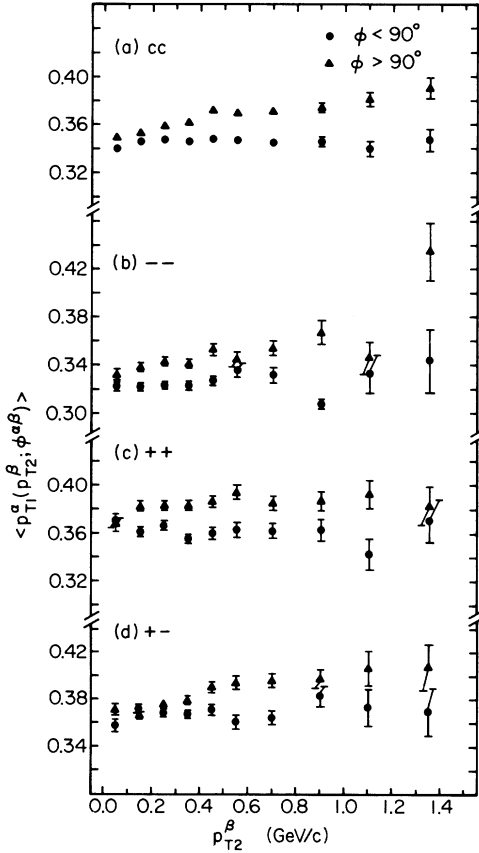


FIG. 31. The average associated transverse momentum,  $\langle p_{T1}^\alpha(p_{T2}^\beta, \phi^{\alpha\beta}) \rangle$  in two  $\phi^{\alpha\beta}$  intervals, for all charge combinations. (The particle at  $p_{T2}$  is not counted in  $\langle p_{T1} \rangle$ .)

The overall increase is due primarily to the opposite-side particles, as the average associated transverse momentum of the same-side particles does not depend on  $p_{T2}^\beta$ . The opposite-side  $\langle p_{T1}^\alpha(p_{T2}^\beta; \phi^{\alpha\beta}) \rangle$  is seen to be larger than the same-side average transverse momentum for all  $p_{T2}^\beta$ . No pronounced differences are observed between the different charge combinations with a possible exception at small  $p_{T2}^\beta$  values.

The results presented in this section were obtained after eliminating the leading particles as described in Sec. IV C. These cuts are not expected to influence the validity of our observations, as they represent mainly low- $p_T$  particles at large rapidity separations.

We conclude with a word of caution. To obtain a complete picture of the event structure in  $p_T$  it is necessary to detect all the neutral particles. Since this is not done in our experiment, conclusions about the way transverse momentum is conserved can be drawn from the results of this section only to the extent to which centrally produced charged particles conserve transverse momentum among themselves. This extent is rather limited, as characterized by the average magnitude of the missing transverse momentum, which in our experiment is  $\sim 0.8$  GeV/c per event.

## V. THREE-PARTICLE DISTRIBUTIONS

Although there exist extensive data on two-particle correlations in high-energy hadron collisions (see Sec. IV), only one other experimental result on three-particle correlations has been reported.<sup>87</sup> In this section, we present our results on three-particle rapidity distributions, where, once again, we integrate over all transverse momenta.

The usual definition of the three-particle correlation function<sup>72</sup> when applied to the semi-inclusive distributions yields

$$C_n^{\alpha\beta\gamma}(y_1^\alpha, y_2^\beta, y_3^\gamma) \equiv \rho_n^{\alpha\beta\gamma}(y_1^\alpha, y_2^\beta, y_3^\gamma) - A_n^{\alpha\beta\gamma}(y_1^\alpha, y_2^\beta, y_3^\gamma), \quad (15)$$

where

$$A_n^{\alpha\beta\gamma}(y_1^\alpha, y_2^\beta, y_3^\gamma) \equiv -2\rho_n^\alpha(y_1^\alpha)\rho_n^\beta(y_2^\beta)\rho_n^\gamma(y_3^\gamma) + \rho_n^{\alpha\beta}(y_1^\alpha, y_2^\beta)\rho_n^\gamma(y_3^\gamma) + \rho_n^{\beta\gamma}(y_2^\beta, y_3^\gamma)\rho_n^\alpha(y_1^\alpha) + \rho_n^{\alpha\gamma}(y_1^\alpha, y_3^\gamma)\rho_n^\beta(y_2^\beta),$$

and  $\rho_n^{\alpha\beta\gamma}$  is the three-particle density,

$$\rho_n^{\alpha\beta\gamma}(y_1^\alpha, y_2^\beta, y_3^\gamma) \equiv \frac{1}{\sigma_n} \frac{d^3\sigma_n}{dy_1^\alpha dy_2^\beta dy_3^\gamma}.$$

The normalization is such that

$$\int \rho_n^{\alpha\beta\gamma}(y_1^\alpha, y_2^\beta, y_3^\gamma) dy_1^\alpha dy_2^\beta dy_3^\gamma = n(\alpha\beta\gamma),$$

where  $n(\alpha\beta\gamma)$  is the number of different combinations of the three particles of types  $\alpha$ ,  $\beta$ , and  $\gamma$  in an event of multiplicity  $n$ .

Analogous to the case of two-particle correlations (Sec. IV A), a correlation function  $\tilde{C}_n$  is defined in terms of particle probability density  $\tilde{\rho}_n$ , i.e.,

$$\tilde{C}_n^{\alpha\beta\gamma}(y_1^\alpha, y_2^\beta, y_3^\gamma) \equiv \tilde{\rho}_n^{\alpha\beta\gamma}(y_1^\alpha, y_2^\beta, y_3^\gamma) - \tilde{A}_n^{\alpha\beta\gamma}(y_1^\alpha, y_2^\beta, y_3^\gamma), \quad (16)$$

where  $\tilde{A}_n$  is obtained from  $A_n$  of Eq. (15) by replacing  $\rho_n$  with  $\tilde{\rho}_n$ . Similar to the one- and two-particle densities,  $\tilde{\rho}_n^{\alpha\beta\gamma}$  is normalized to one over the entire phase space, i.e.,

$$\tilde{\rho}_n^{\alpha\beta\gamma}(y_1^\alpha, y_2^\beta, y_3^\gamma) \equiv \frac{1}{n(\alpha\beta\gamma)} \rho_n^{\alpha\beta\gamma}(y_1^\alpha, y_2^\beta, y_3^\gamma). \quad (17)$$

The inclusive three-particle probability density,  $\tilde{\rho}_n^{\alpha\beta\gamma}(y_1^\alpha, y_2^\beta, y_3^\gamma)$ , is then given by

$$\begin{aligned} C_n^{\alpha\beta\gamma}(y_1^\alpha, y_2^\beta, y_3^\gamma)|_0 = & - \left[ \frac{n(\alpha\beta\gamma)}{n(\alpha)m(\beta)m(\gamma)} - 1 \right] 2\rho_n^\alpha(y_1^\alpha)\rho_n^\beta(y_2^\beta)\rho_n^\gamma(y_3^\gamma) + \left[ \frac{n(\alpha\beta\gamma)}{n(\alpha\beta)m(\gamma)} - 1 \right] \rho_n^{\alpha\beta}(y_1^\alpha, y_2^\beta)\rho_n^\gamma(y_3^\gamma) \\ & + \left[ \frac{n(\alpha\beta\gamma)}{n(\beta\gamma)m(\alpha)} - 1 \right] \rho_n^{\beta\gamma}(y_1^\alpha, y_2^\beta)\rho_n^\alpha(y_3^\gamma) + \left[ \frac{n(\alpha\beta\gamma)}{n(\gamma\alpha)m(\beta)} - 1 \right] \rho_n^{\gamma\alpha}(y_1^\alpha, y_2^\beta)\rho_n^\beta(y_3^\beta). \end{aligned}$$

It is a simple exercise to show that the values of  $C_n^{\alpha\beta\gamma}|_0$  tend to zero for  $n \rightarrow \infty$ . Thus, it is for the small numbers of particles typical of elementary-particle collisions at currently available energies that the introduction of the  $\tilde{C}_n^{\alpha\beta\gamma}$  function is necessary, while  $C_n^{\alpha\beta\gamma}$  is adequate for larger numbers of particles typical of ensembles of atoms and molecules. (This argument holds, of course, also for the relationship between the two-particle correlation functions  $\tilde{C}_n^{\alpha\beta\gamma}$  and  $C_n^{\alpha\beta}$ .)

We have studied semi-inclusive three-particle correlations as defined in Eq. (16) for all multiplicities and for all charge combinations. We find their values to be small; a typical value for  $n \simeq \langle n \rangle$  is  $\tilde{C}_8^{ccc}(0, 0, 0)/\tilde{\rho}_8^{ccc}(0, 0, 0) = 0.006$  ( $|y_i| \leq 0.25$ ,  $i = 1, 2, 3$ ). Note that the corresponding values for two-particle correlations,  $\tilde{C}_8^{cc}(0, 0)/\tilde{\rho}_8^{cc}(0, 0) \simeq 0.14$ , is about 20 times larger (see Sec. IV A). Also, there is a clear regularity observed in the shape of the semi-inclusive two-particle correlations in rapidity (see Sec. IV) which is absent in the three-particle case.<sup>98</sup>

The small values of the three-particle correlation function imply that the semi-inclusive three-particle densities can be expressed in terms of the one- and two-particle densities in the form given by Eq. (21a). For the inclusive three-particle density, we then have

$$\tilde{\rho}_n^{\alpha\beta\gamma}(y_1^\alpha, y_2^\beta, y_3^\gamma) = \sum_n \alpha_n \tilde{\rho}_n^{\alpha\beta\gamma}(y_1^\alpha, y_2^\beta, y_3^\gamma) \quad (18)$$

with

$$\alpha_n = \frac{\sigma_n}{\sigma} \frac{n(\alpha\beta\gamma)}{\langle n(\alpha\beta\gamma) \rangle}, \quad (19)$$

where the average is taken over all multiplicities.

The relationship between the functions  $\tilde{C}_n^{\alpha\beta\gamma}$  and  $C_n^{\alpha\beta\gamma}$  can be illustrated as follows. The condition

$$\tilde{C}_n^{\alpha\beta\gamma}(y_1^\alpha, y_2^\beta, y_3^\gamma) = 0 \quad (20)$$

is satisfied in a sample of events in which the particles are emitted statistically uncorrelated. From Eq. (20) it then follows for the three-particle probability density that

$$\tilde{\rho}_n^{\alpha\beta\gamma}(y_1^\alpha, y_2^\beta, y_3^\gamma) = \tilde{A}_n^{\alpha\beta\gamma}(y_1^\alpha, y_2^\beta, y_3^\gamma). \quad (21a)$$

Equation (17) then yields the corresponding values of  $\rho_n^{\alpha\beta\gamma}$  which, when inserted into Eq. (15), lead to the "no-correlation" value of the function  $C_n^{\alpha\beta\gamma}$ :

$$\tilde{\rho}_n^{\alpha\beta\gamma}(y_1^\alpha, y_2^\beta, y_3^\gamma) = \sum_n \alpha_n \tilde{A}_n^{\alpha\beta\gamma}(y_1^\alpha, y_2^\beta, y_3^\gamma) \quad (21b)$$

with  $\alpha_n$  given by Eq. (19).

In addition, we have tried to find other ways of expressing the three-particle density in terms of the one- and two-particle densities. Among the many possibilities considered, another good approximation is

$$\tilde{\rho}_n^{\alpha\beta\gamma}(y_1^\alpha, y_2^\beta, y_3^\gamma) = \tilde{B}_n^{\alpha\beta\gamma}(y_1^\alpha, y_2^\beta, y_3^\gamma) \quad (22a)$$

and

$$\tilde{\rho}_n^{\alpha\beta\gamma}(y_1^\alpha, y_2^\beta, y_3^\gamma) = \sum_n \alpha_n \tilde{B}_n^{\alpha\beta\gamma}(y_1^\alpha, y_2^\beta, y_3^\gamma) \quad (22b)$$

with

$$\tilde{B}_n^{\alpha\beta\gamma}(y_1^\alpha, y_2^\beta, y_3^\gamma) = \frac{\tilde{\rho}_n^{\alpha\beta}(y_1^\alpha, y_2^\beta)\tilde{\rho}_n^{\beta\gamma}(y_2^\beta, y_3^\gamma)\tilde{\rho}_n^{\gamma\alpha}(y_3^\gamma, y_1^\alpha)}{\tilde{\rho}_n^\alpha(y_1^\alpha)\tilde{\rho}_n^\beta(y_2^\beta)\tilde{\rho}_n^\gamma(y_3^\gamma)}$$

(see Ref. 99). This expression was formulated by Born and Green<sup>100</sup> as a consequence of the superposition assumption of Kirkwood<sup>101</sup> and has been used in the theory of liquids as an ansatz to solve systems of equations for radial distribution functions of molecules in a liquid.

We have tested the validity of both approximations (21) and (22) with our data, and find that both equations describe the data to within a few percent over most of phase space for all multiplicities

$n > 4$  and for all charge combinations. Only when all three particles are together in the center of the rapidity region do we find noticeable disagreement. The difference is largest for three negative particles.

We display our results in Figs. 32 through 34. The bin size of the rapidity  $y_i$  ( $i = 1, 2, 3$ ) in all three figures is 0.5 for  $|y_i| \leq 2.25$ , and 0.9 otherwise.

Figure 32 shows, for  $y_1^\alpha = y_2^\beta = 0$ , the inclusive  $\bar{\rho}^{\alpha\beta\gamma}(y_1^\alpha, y_2^\beta, y_3^\gamma)$  (full circles) as a function of  $y_3^\gamma$  together with the approximations (21b) [dashed line where different from (22b)], and (22b) (solid line) for all charge combinations. As can be seen, the agreement is very good, apart from the deviations mentioned above.

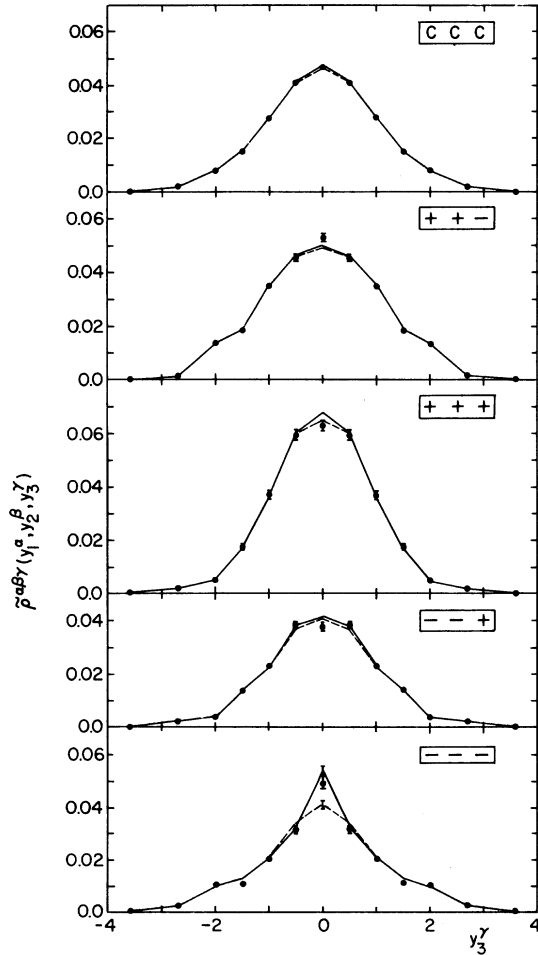


FIG. 32. Inclusive three-particle density  $\bar{\rho}(y_1, y_2, y_3)$  as a function of  $y_3$ , for  $|y_1| \leq 0.25$  and  $|y_2| \leq 0.25$ , for all charge combinations. Full circles represent  $\bar{\rho}$  [Eq. (18)], the solid line the approximation (22b), and the dashed line the approximation (21b) [only shown when it differs from (22b)].

In Fig. 33 we show the validity of the approximations for the inclusive density in the (ccc) case (both positive and negative particles included) over the entire phase space. Again, the agreement is quite good. (The average  $\chi^2$  for the distributions shown in the figure is about 1.6 per degree of freedom.)

We test approximations (21a) and (22a) with our measured semi-inclusive particle densities for the two charge combinations (+ + -) and (- - -) in Fig. 34.

We have found that the three-particle densities at 205 GeV/c can be given in terms of the one- and two-particle densities using either expression (21) or (22). It is difficult to assess to what extent this fact is a reflection of a collision dynamics and to what extent it is influenced by phase-space limitations which become more severe as the number of particles being considered increases. As remarked in the following section, we do not believe a sufficiently realistic Monte Carlo simulation of multiparticle production can be performed at present to study these questions.

We note that the two expressions (21) and (22) become identical when at least one of the three particles is independent of the presence of the two others.

If the validity of the approximation (22) is confirmed with higher statistical accuracy, this will lead to strong conditions on the two-particle densities in the form of an integral equation for  $\bar{\rho}^{\alpha\beta}(y_1^\alpha, y_2^\beta)$  obtained by integrating Eq. (22) over  $y_3^\gamma$ .

## VI. SUMMARY

We summarize here the features of multiparticle production in proton-proton collisions observed in our data:

(i) The pion single-particle inclusive distributions are somewhat flattened in the central region, but no genuine plateau is observed. Approximate scaling in the (target) fragmentation region is observed at beam momenta between 24 and 205 GeV/c.

The form of the semi-inclusive pion rapidity distributions is approximately Gaussian, with the width decreasing and the height increasing with increasing multiplicity.

The pion transverse-momentum distributions change their slope near  $p_T^2 = 0.2$  (GeV/c)<sup>2</sup>, and can be fitted by a sum of two exponentials in  $p_T^2$ . This change in the slope is observed in all multiplicities. A decrease in the low- $p_T^2$  slope of  $Ed^3\sigma/dp^3$  is observed with increasing  $|x|$ , while the slope for  $p_T^2$  above 0.2 (GeV/c)<sup>2</sup> is essentially independent of  $|x|$ .

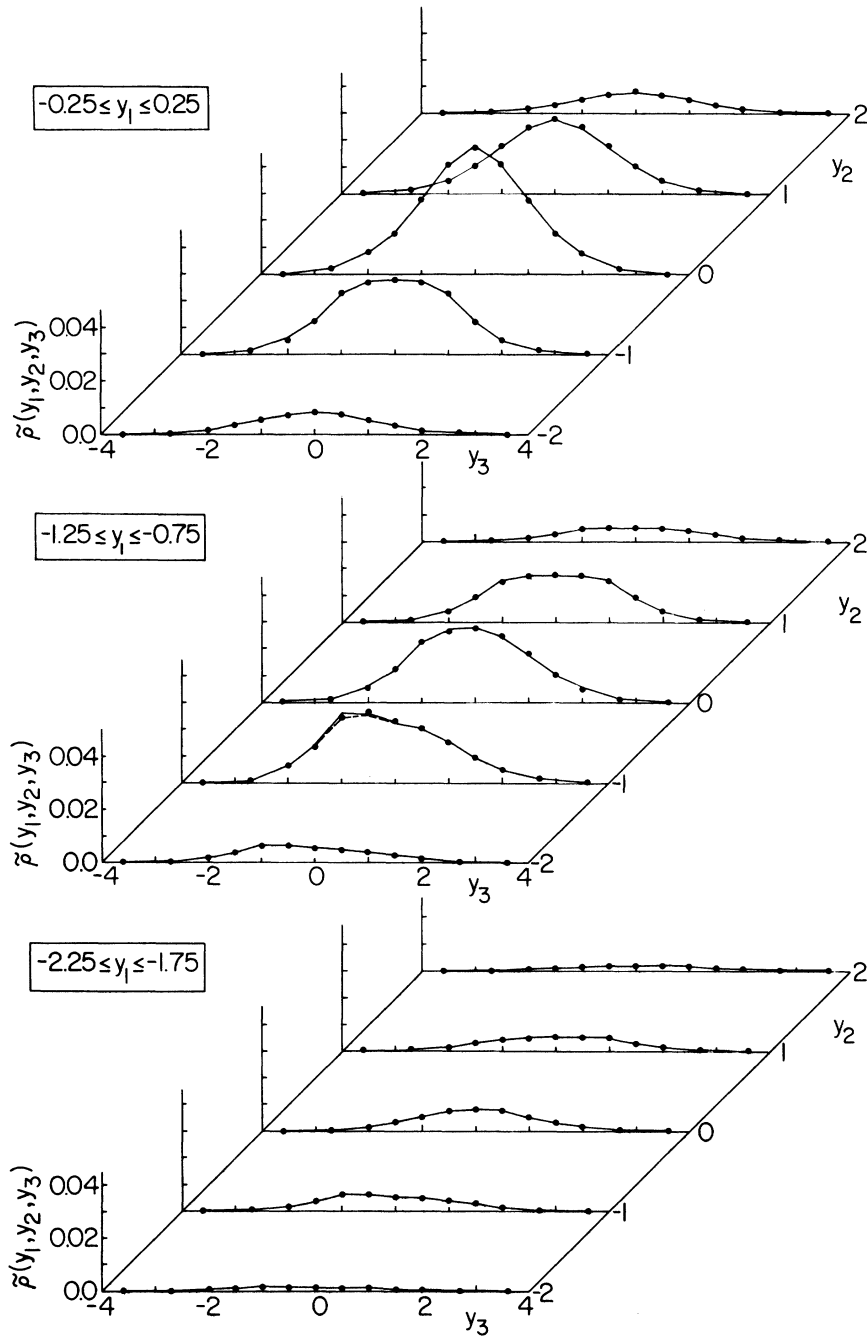


FIG. 33. Inclusive three-particle density  $\tilde{p}(y_1, y_2, y_3)$  for the (ccc) combination, for different values of  $y_1, y_2, y_3$ . The meaning of symbols is the same as in Fig. 32.

The average pion transverse momentum exhibits the so-called sea-gull effect when plotted against the  $x$  or  $x_R$  variables, whereas little dependence of  $\langle p_T \rangle_y$  on  $y$  is observed in the central region. As a function of charged multiplicity,  $\langle p_T \rangle_n$  decreases slowly with increasing  $n$ .

The pion  $x$  distributions can be parametrized by an exponential function over most of the  $x$  inter-

val.

The  $\pi^+$  inclusive cross section is larger than the corresponding  $\pi^-$  cross section. The ratio  $R(\pi^+/\pi^-)$  is 1.15 at its minimum in the central region and increases toward larger  $|y_{c.m.}|$ . As a function of  $p_T^2$ ,  $R(\pi^+/\pi^-)$  is observed to increase with increasing  $p_T^2$ .

(ii) The two-particle distributions were investi-

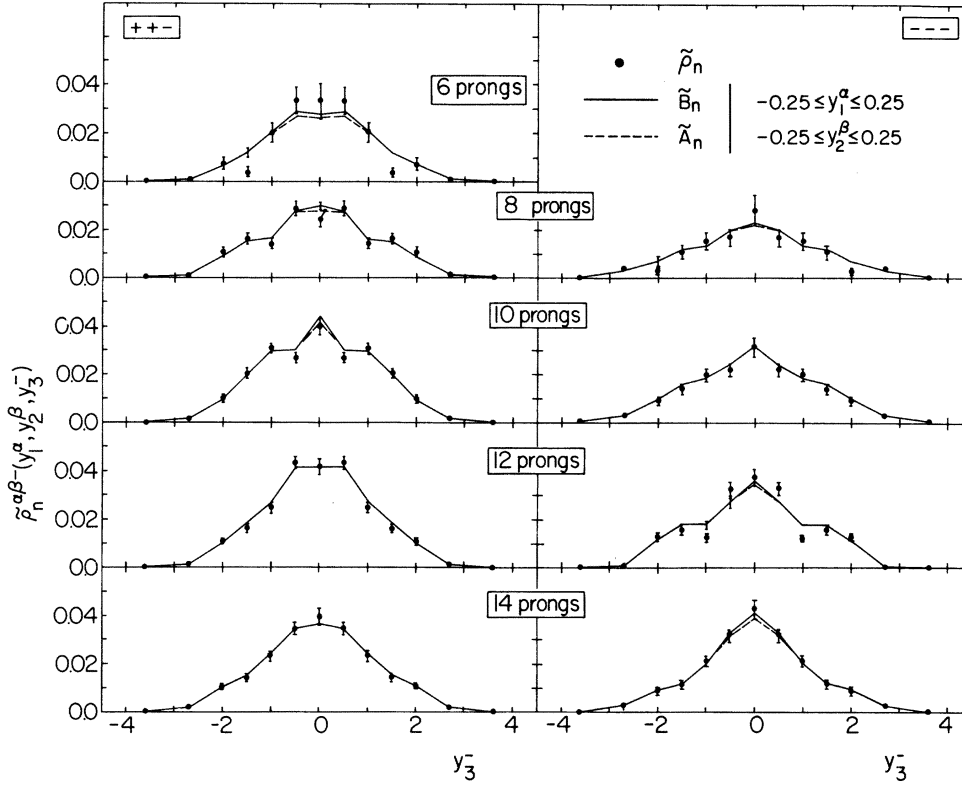


FIG. 34. Semi-inclusive three-particle densities  $\tilde{\rho}_n(y_1, y_2, y_3)$  as a function of  $y_3$  for the charge combinations  $(++-)$  and  $(---)$  and for  $|y_1| \leq 0.25$ ,  $|y_2| \leq 0.25$ . The solid and dashed lines represent the approximations (22a) and (21a), respectively.

gated using the correlation function formalism. The inclusive correlation function can be written as a sum of the average semi-inclusive correlation function and a term containing single-particle distributions only. It is the latter term which determines the magnitude and shape of the inclusive correlation function in the central region.

A shape characteristic of short-range correlations is observed in the semi-inclusive correlation functions  $\tilde{C}_n^{\alpha\beta}(y_1^\alpha, y_2^\beta)$  in the  $+-$  and  $cc$  charge combinations. The dependence of  $\tilde{C}_n^{\alpha\beta}(y_1^\alpha, y_2^\beta)$  on  $\frac{1}{2}(y_1^\alpha - y_2^\beta)$  can be parametrized in a way motivated by the independent-cluster-emission model.

A striking difference is observed between the  $---$  and  $+-$  charge combinations in the joint correlation function in rapidity and the azimuthal angle. The function  $\tilde{C}_n^{+-}(y_1^+, y_2^-, \phi^{+-})$  has a maximum at  $y_1 = y_2 = 0$  for  $\phi^{+-}$  close to  $180^\circ$ , while  $\tilde{C}_n^{--}(y_1^-, y_2^-, \phi^{--})$  has a maximum for  $\phi^{--}$  close to  $0^\circ$ . We interpret this difference in  $\phi$  dependence of short-range correlations to be, at least in part, a consequence of two different dynamical mechanisms: resonance production in the  $+-$  case (a  $\rho^0$  signal has been observed in our data), and Bose-Einstein statistics in the  $---$  case.

No definite dynamical effects are observed in the semi-inclusive correlation functions in  $p_T$ . The average multiplicity associated with the magnitude of the transverse momentum of a particle has been used as a convenient quantity characterizing both the inclusive and the semi-inclusive  $p_T$  correlations. The associated multiplicity of the same-side ( $\phi < 90^\circ$ ) particles dominates the  $---$  combination at small  $\Delta y$  and small  $p_T$ , while the opposite-side ( $\phi > 90^\circ$ ) multiplicity is the larger one for the  $+-$  combination in the same region. Overall, it is observed that both the opposite-side average associated multiplicity and the average associated transverse momentum are larger than their same-side values.

Definitive understanding of the dynamics of multiparticle production cannot be reached without adequate knowledge of the production of neutral particles. It is likely that at least a part of the observed semi-inclusive correlations is due to the mixing of events with various total multiplicities characterized by different single-particle distributions.

(iii) No definite three-particle correlations were observed. In fact, two different ways of expres-

sing the three-particle densities in terms of one- and two-particle densities were found, Eq. (21a) and Eq. (22a).

Last, we comment on a point of prime importance regarding the identification of dynamical effects in the data on correlation functions. Before one can make valid conclusions about the presence of any dynamical effects, one should identify and subtract any effects of kinematic origin. This has not yet been done in a convincing way. The customary method is to compare data with results of a Monte Carlo calculation based on a model incorporating only those features of the data which are not considered to be a direct consequence of any dynamical correlations, notably the momentum and energy conservation, and the single-particle distributions (either in  $p_T$  only, or both in  $p_T$  and  $p_\perp$ ). The results differ as much as do the individual Monte Carlo programming techniques and the assumptions necessary to fill in the gaps in the data used as an input for such calculations. The latter present currently a serious problem, as neither the multiplicity distribution of neutral pions (for fixed number of charged particles) nor the semi-inclusive single-particle

distributions of leading particles are known experimentally in sufficient detail. We shall therefore defer to the future any improvements from our previously published report on this aspect of the analysis.<sup>19</sup>

#### ACKNOWLEDGMENTS

We express our appreciation to the staff of the Fermi National Accelerator Laboratory, and especially the Bubble Chamber staff, for their aid with the experimental run. We thank the scanning staffs of the Argonne National Laboratory and the State University of New York at Stony Brook for scanning and measuring the film. We are indebted to S. J. Barish, D. Colley, M. Derrick, B. Musgrave, P. A. Schreiner, and H. Yuta from ANL for supplying data on the complete sample of inelastic two- and four-prong events. It is a pleasure to acknowledge helpful discussions with E. L. Berger, D. Campbell, P. Grannis, F. Hayot, M. Holder, A. Krzywicki, B. McCoy, K. McDonald, B. Oh, C. Quigg, G. H. Thomas, J. M. Wang, T. T. Wu, and C. N. Yang.

\*Present address: Michigan State University, East Lansing, Michigan 48823.

†On leave of absence from CERN, Geneva, Switzerland.

‡Work supported in part by the National Science Foundation.

§Work supported by the United States Energy Research and Development Administration.

<sup>1</sup>D. Horn, Phys. Rep. 4, 1 (1972); W. R. Frazer *et al.*, Rev. Mod. Phys. 44, 284 (1972); K. Gottfried, Report No. Ref.TH.1615, CERN, 1973 (unpublished); M. Jacob, Report No. Ref.TH.1683, 1973 (unpublished); E. L. Berger, Report No. Ref.TH.1737, CERN, 1973 (unpublished); D. Horn and F. Zachariassen, *Hadron Physics at Very High Energies* (Benjamin, Reading, Mass., 1973).

<sup>2</sup>G. Charlton *et al.*, Phys. Rev. Lett. 29, 515 (1972).

<sup>3</sup>S. J. Barish *et al.*, Phys. Rev. D 9, 2689 (1974).

<sup>4</sup>S. J. Barish *et al.*, Phys. Rev. D 9, 1171 (1974).

<sup>5</sup>S. Barshay *et al.*, Phys. Rev. Lett. 32, 1390 (1974).

<sup>6</sup>J. Whitmore and M. Derrick, Phys. Lett. 50B, 280 (1974).

<sup>7</sup>S. J. Barish *et al.*, Phys. Rev. Lett. 31, 1080 (1973).

<sup>8</sup>J. Whitmore *et al.*, Phys. Rev. D 11, 3124 (1975).

<sup>9</sup>M. Derrick *et al.*, Phys. Rev. D 9, 1853 (1974).

<sup>10</sup>M. Derrick *et al.*, Phys. Rev. D 9, 1215 (1974).

<sup>11</sup>M. Derrick *et al.*, Phys. Rev. Lett. 32, 80 (1974).

<sup>12</sup>G. Charlton *et al.*, Phys. Rev. Lett. 30, 574 (1973).

<sup>13</sup>G. Charlton *et al.*, Phys. Rev. Lett. 29, 1759 (1972).

<sup>14</sup>K. Jaeger *et al.*, Phys. Rev. D 11, 2405 (1975).

<sup>15</sup>Y. Cho *et al.*, Phys. Rev. Lett. 31, 413 (1973).

<sup>16</sup>Z. M. Ma *et al.*, Phys. Rev. Lett. 31, 1320 (1973).

<sup>17</sup>T. F. Hoang and R. Singer, Report No. ANL/HEP 7455,

Argonne National Laboratory, 1975 (unpublished).

<sup>18</sup>T. Ludlam *et al.*, Phys. Lett. 48B, 449 (1974).

<sup>19</sup>R. Singer *et al.*, Phys. Lett. 49B, 481 (1974).

<sup>20</sup>M. Pratap *et al.*, Phys. Rev. Lett. 33, 797 (1974).

<sup>21</sup>R. G. Glasser *et al.*, Phys. Lett. 53B, 387 (1974).

<sup>22</sup>E. L. Berger *et al.*, Phys. Rev. D 15, 206 (1977).

<sup>23</sup>T. Kafka *et al.*, Phys. Rev. Lett. 34, 687 (1975).

<sup>24</sup>P. Pirilä, G. H. Thomas, and C. Quigg, Phys. Rev. D 12, 92 (1975).

<sup>25</sup>S. J. Barish *et al.*, Phys. Rev. D 12, 1260 (1975).

<sup>26</sup>R. Singer *et al.*, Phys. Lett. 60B, 385 (1976).

<sup>27</sup>F. Beck, Report No. ANL/HEP 7128, Argonne National Laboratory, 1971 (unpublished); F. Beck *et al.*, Proceedings of the Informal Colloquium on POLLY and POLLY-like Devices, Report No. ANL/HEP 7934, Argonne National Laboratory, 1972 (unpublished).

<sup>28</sup>F. T. Solmitz, A. D. Johnson, and T. B. Day, Alvarez Group Programming No. P-117, University of California, Lawrence Radiation Laboratory, Berkeley, 1966 (unpublished).

<sup>29</sup>C. I. Dahl, T. B. Day, F. T. Solmitz, and N. L. Gould, Group A Programming No. P-126, University of California, Lawrence Radiation Laboratory, Berkeley, 1968 (unpublished).

<sup>30</sup>The bubble-pattern matching method was conceived by T. Fields and first tested at ANL.

<sup>31</sup>M. Antinucci *et al.*, Lett. Nuovo Cimento 6, 121 (1973).

<sup>32</sup>This corresponds to the major part of the region  $p_{lab} \leq 1.4$  GeV/c.

<sup>33</sup>M. Banner *et al.*, Phys. Lett. 41B, 547 (1972).

<sup>34</sup>A. Bertin *et al.*, Phys. Lett. 38B, 260 (1972).

<sup>35</sup>A. Bertin *et al.*, Phys. Lett. 41B, 201 (1972).

- <sup>36</sup>A. Bertin *et al.*, Phys. Lett. **42B**, 493 (1972).
- <sup>37</sup>P. Capiluppi *et al.*, Nucl. Phys. **B70**, 1 (1974).
- <sup>38</sup>P. Capiluppi *et al.*, Nucl. Phys. **B79**, 189 (1974).
- <sup>39</sup>E. Albini *et al.*, NPI Internal Report No. 75-2, CERN, 1975 (unpublished).
- <sup>40</sup>B. Alper *et al.*, Phys. Lett. **47B**, 75 (1973).
- <sup>41</sup>B. Alper *et al.*, Nucl. Phys. **B100**, 237 (1975). Also, B. Duff (private communication).
- <sup>42</sup>M. G. Albrow *et al.*, Phys. Lett. **40B**, 136 (1972).
- <sup>43</sup>M. G. Albrow *et al.*, Phys. Lett. **42B**, 279 (1972).
- <sup>44</sup>M. G. Albrow *et al.*, Nucl. Phys. **B51**, 388 (1973).
- <sup>45</sup>M. G. Albrow *et al.*, Nucl. Phys. **B54**, 6 (1973).
- <sup>46</sup>M. G. Albrow *et al.*, Nucl. Phys. **B56**, 333 (1973).
- <sup>47</sup>M. G. Albrow *et al.*, Nucl. Phys. **B73**, 40 (1974).
- <sup>48</sup>We have used the ISR results at the lowest ISR energy,  $\sqrt{s} = 23$  GeV, which is higher than  $\sqrt{s} = 19.7$  GeV of this experiment. Since the average multiplicity of kaons, and especially antiprotons, increases with  $s$  faster than the pion multiplicity, using higher-energy data means that our  $K$  and  $\bar{p}$  background is slightly over-estimated.
- <sup>49</sup>A simplification of data suggested by several ISR experiments (Refs. 38, 41, and 50) covering limited  $x$  intervals. It leads to underestimating slightly the proton background. However, we feel it is sufficient for the intended purpose.
- <sup>50</sup>J. C. Sens, Ann. N. Y. Acad. Sci. **229**, 189 (1974).
- <sup>51</sup>N. M. Kroll and W. Wada, Phys. Rev. **98**, 1355 (1955).
- <sup>52</sup>Unless noted otherwise, the data points for all rapidity distributions shown in Sec. III were obtained using a bin size of 0.4 units in rapidity.
- <sup>53</sup>The  $90^\circ$  production angle in the c.m.s. ( $y_{c.m.} = 0$ ) corresponds to the laboratory rapidity  $y_{lab} = 3.04$  in the 205-GeV/c  $pp$  collisions.
- <sup>54</sup>R. S. Panvini *et al.*, Phys. Lett. **38B**, 55 (1972).
- <sup>55</sup>W. H. Sims *et al.*, Nucl. Phys. **B41**, 317 (1972).
- <sup>56</sup>V. Blobel *et al.*, Nucl. Phys. **B69**, 454 (1974).
- <sup>57</sup>V. A. Bumazhnov *et al.*, Phys. Lett. **50B**, 283 (1974).
- <sup>58</sup>C. Bromberg *et al.*, Phys. Rev. D **9**, 1864 (1974).
- <sup>59</sup>C. Bromberg *et al.*, Nucl. Phys. **B107**, 82 (1976).
- <sup>60</sup>Owing to the symmetry of the  $pp$  system, all distributions in c.m. longitudinal momentum must be symmetric with respect to  $x = y_{c.m.} = 0$ . [The same holds for distributions in  $y_{lab}$ , as rapidity distributions are invariant under Lorentz transformations in the longitudinal (beam) direction.] The presence or absence of symmetry in Fig. 3 is therefore a measure of the quality (or lack thereof) of the measurement and of the correction procedures. In Fig. 4 and the following figures (as well as in Secs. IV and V), the c.m. symmetry is imposed by symmetrizing the distributions about  $x = y_{c.m.} = 0$ .
- <sup>61</sup>For  $y_{lab} \approx 0$  the data suggest that the cross section decreases with increasing energy. Published analyses (Refs. 62 and 63) have shown that the data for pion production in the fragmentation region in  $pp$  interactions are compatible with an  $s^{-1/2}$  energy dependence for  $p_{lab} > 30$  GeV/c. An attempt to examine the  $s$  dependence of  $d\sigma/dy|_{y=const}$  for  $y$  in the central region more quantitatively shows that the data cannot distinguish between the  $s^{-1/4}$  and the  $s^{-1/2}$  rate of approach to asymptotic behavior at the present accuracy of the experiments. [See A. M. Rossi *et al.*, Nucl. Phys. **B84**, 269 (1975).]
- <sup>62</sup>R. Schindler *et al.*, Phys. Rev. Lett. **33**, 862 (1974).
- <sup>63</sup>J. Whitmore *et al.*, Phys. Lett. **60B**, 211 (1976).
- <sup>64</sup>Differences in normalization can be observed among different ISR experiments themselves. However, when the energy dependence is studied using data from a single experiment, no variations of energy dependence of the central cross section with transverse momentum have been found (see Ref. 33).
- <sup>65</sup>P. Basetti *et al.*, Nucl. Phys. **B62**, 46 (1973).
- <sup>66</sup>The results displayed in Fig. 7 were obtained by applying to the data the same cuts as those used later in Secs. IV and V (see Sec. IV C). No corrections were applied.
- <sup>67</sup>S. Barshay and Y. A. Chao, Phys. Lett. **38B**, 225 (1972).
- <sup>68</sup>R. Hagedorn and J. Ranft, Suppl. Nuovo Cimento **6**, 169 (1968).
- <sup>69</sup>S. Z. Belenkij and L. D. Landau, Suppl. Nuovo Cimento **3**, 15 (1956); Minh Duong-van and P. Carruthers, Phys. Rev. Lett. **31**, 133 (1973).
- <sup>70</sup>Here  $\langle p_T \rangle_a$  denotes the average value of  $p_T$  obtained from a set of particles characterized by a value of the variable  $a$  which lies within a given interval.
- <sup>71</sup>M. Bardadin *et al.*, in *Proceedings of the Siena International Conference on Elementary Particles*, edited by G. Bernardini and G. P. Puppi (Società Italiana di Fisica, Bologna, Italy, 1963), Vol. I, p. 628.
- <sup>72</sup>A. H. Mueller, Phys. Rev. D **2**, 2963 (1970); **4**, 150 (1971).
- <sup>73</sup>K. G. Wilson, Report No. CLNS-131, Cornell University, Ithaca, N.Y., 1970 (unpublished).
- <sup>74</sup>S. R. Amendolia *et al.*, Phys. Lett. **48B**, 359 (1974).
- <sup>75</sup>The figure is included for illustration only. It represents data obtained by eliminating leading particles which were taken to be all positive particles with  $|x| > 0.6$ .
- <sup>76</sup>The symmetry with respect to the line  $y_1 = y_2$  is a consequence of the symmetry of the  $pp$  system, and the symmetry with respect to the line  $y_1 = -y_2$  is present whenever correlations among particles of the same type ( $cc$ ,  $--$ , or  $++$ ) are considered.
- <sup>77</sup>W. Ko, Phys. Rev. Lett. **28**, 935 (1972).
- <sup>78</sup>A. Białas, in *Proceedings of the IV International Symposium on Multiparticle Hadrodynamics, Pavia, Italy, 1973*, edited by F. Dulmio *et al.* (INFN, Pavia, 1974), p. 93.
- <sup>79</sup>The relation between inclusive correlation functions and the semi-inclusive distributions was also investigated in R. Slansky, Nucl. Phys. **B73**, 477 (1974).
- <sup>80</sup>C. Quigg, in *Proceedings of the Canadian Institute for Particle Physics Summer School, McGill University, 1973*, edited by R. Henzi and B. Margolis (McGill University, Montreal, 1973), p. 517.
- <sup>81</sup>Note that the plots are symmetric for  $y_1 + y_2 \neq 0$  for like-particle combinations only.
- <sup>82</sup>Preliminary results on semi-inclusive two-particle correlations from this experiment were published using a data sample half the present size (see Ref. 19). This necessitated using a larger bin size ( $\Delta y = 1.0$ ) obscuring some fine structure in the correlation function. (Also, the  $R$  functions were used in Ref. 19.) However, we believe that our previous analysis is consistent with the results presented here.
- <sup>83</sup>J. Erwin *et al.*, Phys. Rev. Lett. **33**, 1443 (1974).
- <sup>84</sup>D. Bogert *et al.*, paper presented at the Annual Meeting of the American Physical Society, Anaheim, California, 1975 [Bull. Am. Phys. Soc. **20**, 14 (1975)].

- <sup>85</sup>B. Y. Oh *et al.*, Phys. Lett. **56B**, 400 (1975).
- <sup>86</sup>N. N. Biswas *et al.*, Phys. Rev. Lett. **35**, 1059 (1975).
- <sup>87</sup>K. Eggert *et al.*, Nucl. Phys. **B86**, 201 (1975).
- <sup>88</sup>S. R. Amendolia *et al.*, Nuovo Cimento **31A**, 17 (1976).
- <sup>89</sup>E. L. Berger, Nucl. Phys. **B85**, 61 (1975).
- <sup>90</sup>F. Hayot, Lett. Nuovo Cimento **12**, 676 (1975). The first attempt to give a more quantitative connection between resonance production and correlations can be found in: A. Gula, Report No. RL-75-080, Rutherford Laboratory, Chilton, Didcot, United Kingdom, 1975 (unpublished).
- <sup>91</sup>Recently, an explicit calculation based on the dual model has also shown that a two-body decay of a resonance leads to a peak in the correlation function for  $\phi$  close to  $180^\circ$ , while a three-body decay of a resonance yields a peak for  $\phi$  close to  $0^\circ$ . See A. DiGiacomo, Phys. Lett. **60B**, 276 (1976).
- <sup>92</sup>G. Goldhaber *et al.*, Phys. Rev. **120**, 300 (1960).
- <sup>93</sup>D. Sivers, S. J. Brodsky, and R. Blankenbecler, Phys. Rep. **23C**, 1 (1976).
- <sup>94</sup>H. T. Nieh and J. M. Wang, Phys. Rev. D **5**, 2226 (1972).
- <sup>95</sup>M. Pratap and J. Schlesinger, Report No. PNPE 106, Universite d l'Etat, Mons, Belgium, 1975 (unpublished).
- <sup>96</sup>The bin sizes in  $p_T$  used in Figs. 29 through 31 were 0.1 GeV/c for  $p_T < 0.6$  GeV/c, and 0.2 GeV/c for  $0.6 < p_T < 1.2$  GeV/c. The last bin is from 1.2 to 1.5 GeV/c.
- <sup>97</sup>J. Derre *et al.*, Report No. IHEP 75-99, Institute of High Energy Physics, Serpukhov, 1975 (unpublished).
- <sup>98</sup>We note that a  $\rho^0$  signal has been detected in our  $(\pi^+\pi^-)$  invariant-mass distribution (see Ref. 26), but no structure has been observed in the three-particle-invariant-mass distributions. The observed number of  $\rho^0$  per inelastic event,  $0.33 \pm 0.06$ , corresponds to the signal-to-background ratio of only 1 : 6. The multiplicity of heavier particles which would decay into three charged pions, such as  $A_2$ , is expected to be smaller, and the combinatorial background is expected to be larger to such an extent as to render the presence of such a particle in our data undetectable.
- <sup>99</sup>T. Kafka *et al.*, State University of New York at Stony Brook Report No. SUNY SB-BCG-2/75, 1975 (unpublished).
- <sup>100</sup>M. Born and H. S. Green, Proc. R. Soc. London **A188**, 10 (1946); *A General Kinetic Theory of Liquids* (Cambridge Univ. Press, Cambridge, England, 1949).
- <sup>101</sup>J. G. Kirkwood, J. Chem. Phys. **3**, 300 (1935); J. G. Kirkwood and E. M. Baggs, *ibid.* **10**, 394 (1942).
- <sup>102</sup>B. Oh *et al.*, Nucl. Phys. B **116**, 13 (1976).